advances in carbon neutrality

MDPI

Review

Electrolyte-Dependent Roles of Metallic Nanoparticles in Electrochemical CO_2 Reduction to CO

William Murphcoux, Daralyn Plascencia and Luis González-Urbina *

Department of Science, Borough of Manhattan Community College, City University of New York, New York, NY 10007, USA
* Correspondence: lgonzalezurbina@bmcc.cuny.edu

Abstract

The electrochemical reduction of carbon dioxide (CO_2) to carbon monoxide (CO) is a promising strategy for converting a greenhouse gas into a valuable chemical feedstock. Metallic nanoparticles provide a versatile platform for tuning catalytic activity and selectivity through control of size, morphology, composition, and surface electronic structure. However, their performance is strongly dependent on the electrolyte environment, which governs reaction pathways, intermediate stabilization, mass transport, and competing side reactions. This review examines metallic nanoparticle catalysts for CO_2-to-CO electroreduction across aqueous electrolytes, ionic liquids, and molten salts. Emphasis is placed on how each medium modifies nanoparticle behavior: aqueous systems are governed by proton-coupled electron transfer and competition with hydrogen evolution; ionic liquids can stabilize activated CO_2-derived species and modify the electric double layer; and molten salts operate through high-temperature carbonate- and oxide-ion chemistry. The review further compares nanoparticle design strategies, transport and stability limitations, and the extent to which catalyst and electrolyte effects can be distinguished. Nanoparticle performance cannot be separated from the electrolyte environment. Catalyst composition and structure must therefore be considered together with electrolyte-dependent effects on reactant availability, intermediate stabilization, and competing reactions.

Keywords: CO_2 reduction; CO production; nanoparticles

1. Introduction

The electrochemical reduction of carbon dioxide has a history spanning more than a century, with early qualitative observations dating back to the late nineteenth century [1]. In 1870, Royer reported the conversion of carbonic acid to formic acid using a zinc electrode [2]. Since then, a steady progression in the field has been marked by pivotal studies: in the mid-1980s, Hori et al. performed systematic investigations of metal cathodes in aqueous bicarbonate electrolytes, and established that metals such as Ag and Au produced CO while Cu uniquely afforded hydrocarbons, including CH_4 [3]. Building on this foundational work, the subsequent decades have seen extensive research into catalyst design, mechanistic pathways, and product selectivity for CO_2 electroreduction [4].

While CO_2 reduction has been studied for decades, carbon capture and storage is a relatively recent concept, first appearing in the late 1970s [5]. Today, the urgency of mitigating greenhouse gas emissions has renewed interest in innovative approaches, including electrochemical carbon capture [6]. Nevertheless, the long-term viability of these solutions remains fundamentally tied to economics: without cost-effective implementation, even the

Check for updates

Academic Editor: John Bell

Received: 20 July 2026
Revised: 8 October 2026
Accepted: 15 October 2026
Published: 1 November 2026

Copyright: © 2026 by the authors. Licensee MDPI, Basel, Switzerland. This article is an open access article distributed under the terms and conditions of the Creative Commons Attribution (CC BY) license.

most technically advanced capture strategies are unlikely to scale beyond experimental or niche applications.

Carbon monoxide is a highly versatile chemical with a range of industrial applications, primarily as a building block for the synthesis of fuels, chemicals, and polymers [7,8]. It is used extensively in the production of methanol, acetic acid, and various hydrocarbons through processes such as the Fischer–Tropsch synthesis [9]. CO also serves as a reducing agent in metal processing and as a feedstock for carbonylation reactions in the pharmaceutical and fine chemical industries. The global market for carbon monoxide is significant, driven by demand from energy, chemical, and manufacturing sectors. While CO is not traded as a commodity in the same way as natural gas or crude oil, its economic value is closely linked to its industrial uses. The CO market is projected to reach USD 6.97 billion by 2030 [10,11], reflecting both the scale of chemical production and emerging interest in CO utilization from renewable or captured CO_2 sources (Figure 1).

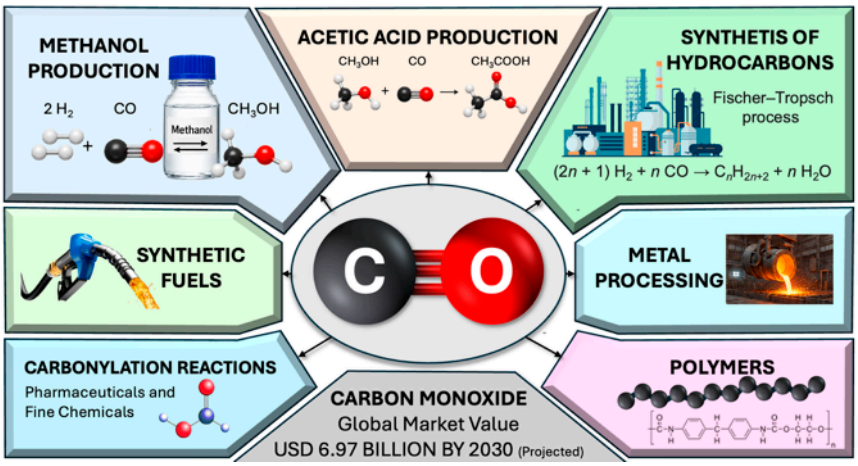


Figure 1. Industrial applications of carbon monoxide. As a key intermediate in modern chemical manufacturing, CO can be converted into fuels and value-added chemicals, illustrating the potential impact of sustainable CO production through electrochemical CO_2 reduction.

Building on these foundational metal-dependent selectivity relationships, advances in electrolytic techniques since the 2000s, including gas-diffusion electrodes and membrane–electrode assemblies, have enabled industrially relevant current densities and energy efficiencies, transforming CO_2-to-CO electrolysis from a scientific curiosity into a key pathway for sustainable fuel and chemical production [12–15]. In recent years, the development of nanostructured catalysts has further accelerated progress by increasing activity, improving CO selectivity, and reducing the overpotential required for CO_2 electroreduction.

Electrochemical reduction of CO_2 has been demonstrated in a variety of electrolyte media, each offering distinct mechanistic and selectivity characteristics. In aqueous electrolytes, proton availability enables hydrogenation pathways leading to products such as CO, formate, and hydrocarbons, although the competing hydrogen evolution reaction (HER) often limits selectivity [16]. Ionic liquids have emerged as promising alternatives because their high CO_2 solubility and wide electrochemical windows can suppress HER and stabilize CO_2^- intermediates, enhancing Faradaic efficiency toward CO or formate [17–19]. In contrast, molten carbonate or oxide electrolytes allow CO_2 electrolysis at elevated temperatures, where ionic conductivity and reaction kinetics are improved, enabling direct formation of CO and solid carbon with high current densities [20–22]. Catalyst-surface interactions with key reaction intermediates also determine overpotential, activity, and product selectivity. Nanostructuring provides an additional level of control through particle size, morphology, composition, surface coordination, and electronic structure, allowing

the catalyst–electrolyte interface to be engineered toward improved activity and selective CO production.

Herein, we summarize recent advances in electrochemical CO_2 reduction to CO, with particular focus on metallic nanoparticle catalysts in aqueous solutions, ionic liquids, and molten salts. Using the electrolyte environment as the organizing framework, we examine how nanoparticle composition, structure, surface chemistry, and stability interact with electrolyte-dependent reaction mechanisms, interfacial organization, mass transport, and operating conditions. Focusing specifically on CO production provides a common reaction pathway through which these coupled catalyst–electrolyte effects can be compared across fundamentally different media.

2. Catalyst–Electrolyte Interactions: A Conceptual Framework

2.1. Electrolyte Properties

Before considering how nanoparticle structure influences CO_2 reduction, it is necessary to define the chemical environment in which the catalyst operates. The electrolyte influences the availability and transport of reactive species and the reaction pathways accessible at the catalyst surface. Consequently, the same catalyst may exhibit different activity and selectivity depending on the surrounding medium. Proton availability is particularly important: aqueous electrolytes support proton-coupled electron-transfer pathways but also promote the competing hydrogen evolution reaction, whereas nominally aprotic environments restrict proton availability and can substantially alter the reduction mechanism. Ionic liquids offer additional control through their tunable composition and water content, while nominally anhydrous molten salts favor fundamentally different, oxide-ion-mediated chemistry. The contrasting CO_2-to-CO reaction environments in aqueous solutions, ionic liquids, and molten salts are illustrated schematically in Figure 2.

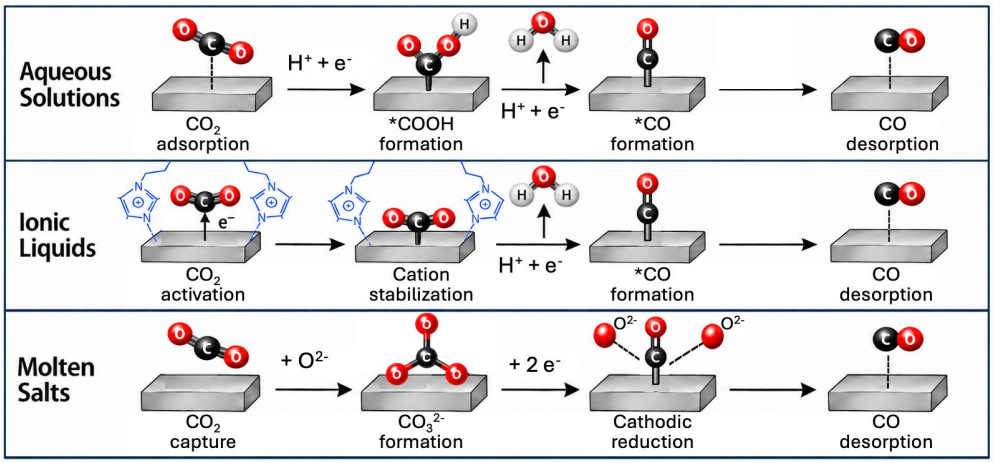


Figure 2. Schematic representation of cathodic CO_2-to-CO reaction pathways in aqueous, ionic-liquid, and molten salt media. (*) denotes an intermediate adsorbed on the catalyst surface.

Other electrolyte properties—including CO_2 concentration and speciation, ion identity, conductivity, viscosity, solvation, and operating temperature—also influence reaction kinetics and mass transport. Together, these factors determine the local environment experienced by the nanoparticle and therefore provide the first level of control over catalytic performance.

2.2. Nanoparticle Properties

Metallic nanoparticles combine the intrinsic electronic properties of metals with size-dependent geometric and electronic effects. Parameters such as elemental composition, particle size, exposed crystal facets, and the density of low-coordination sites determine the number and nature of catalytically active sites. At the nanoscale, altered coordination environments, lattice strain, and changes in electronic structure can modify CO_2 activation and the binding energies of key reaction intermediates. These properties can be further tuned through alloying, oxidation state, surface functionalization, and interactions with catalyst supports.

Together, these characteristics govern the stabilization and desorption of intermediates such as *COOH and *CO and therefore influence catalytic activity and selectivity. Nanoparticle structure, however, does not determine performance in isolation: interfacial electric fields, local solvation, ion adsorption, and mass transport within the surrounding electrolyte determine how these nanoscale properties are expressed under operating conditions. Throughout this review, an asterisk (*) preceding a chemical species denotes an intermediate adsorbed on the catalyst surface.

2.3. Interfacial Consequences

At the catalyst–electrolyte boundary, the electronic properties of the nanoparticle interact with the organization of ions and solvent molecules within the electrochemical interface. Surface curvature, low-coordination sites, and structural defects can modify local charge density, while the composition and organization of the electrolyte determine the distribution of ions and the resulting interfacial electric field. These coupled effects influence local CO_2 concentration, proton availability, solvation, and access of reactive species to catalytic sites. Moreover, nanoparticle surfaces are not necessarily static under electrochemical polarization and may undergo changes in coordination, oxidation state, or surface structure during operation.

These interfacial effects directly influence CO_2 activation and the stabilization, transformation, and desorption of reaction intermediates. Electric fields, specific ion adsorption, and local solvation environments can modify intermediate binding energies and therefore alter reaction kinetics and product selectivity. Their importance differs among electrolyte systems: in aqueous media, interfacial water structure, local pH, and ion adsorption influence the competition between CO_2 reduction and hydrogen evolution; in ionic liquids, strong ionic organization and cation–intermediate interactions can substantially alter CO_2 activation; and in molten salts, oxide-ion transport and high-temperature interfacial chemistry introduce a distinct set of constraints. Thus, catalytic performance emerges from the interaction between nanoparticle structure and the surrounding electrolyte rather than from either component independently.

2.4. Catalytic Performance and Comparability

The performance of CO_2 reduction electrocatalysts is commonly evaluated using overpotential, current density, Faradaic efficiency, turnover frequency (TOF), and stability. Overpotential describes the additional potential beyond the thermodynamic equilibrium potential required to drive the reaction, while current density (j) reflects the rate of electrochemical conversion. Geometric current density is particularly relevant to practical productivity, whereas normalization to the electrochemically active surface area (ECSA) can provide additional information about intrinsic surface activity. Partial current density toward a specific product, such as CO (j_{CO}), combines the overall reaction rate with product selectivity. Faradaic efficiency quantifies the fraction of charge directed toward a specific product; the Faradaic efficiency toward CO is denoted FE_{CO}. TOF can provide a site-specific

activity measure when the number of active sites can be reliably estimated, whereas mass activity normalizes the catalytic current to the mass of catalyst.

These metrics, however, are strongly influenced by experimental conditions. Electrode architecture, catalyst loading, reactor configuration, mass transport, electrolyte resistance, and local concentration or pH gradients can substantially alter measured current densities and operating potentials independently of the intrinsic properties of the catalyst. Gas-diffusion electrodes, for example, may achieve much higher current densities than planar electrodes primarily because they improve CO_2 transport to the catalyst surface.

Consequently, performance values reported under different electrolyte and reactor conditions should be compared with caution. This limitation becomes particularly important when comparing aqueous electrolytes, ionic liquids, and molten salts, which differ substantially in operating temperature, CO_2 availability, transport properties, interfacial structure, and potential reference conventions. Cross-electrolyte comparisons are therefore most informative when used to identify trends and design principles rather than simple numerical rankings of catalyst performance.

3. Aqueous Electrolytes

The primary advantages of aqueous electrolytes are their mild operating conditions, low electrolyte cost, widespread availability, and established handling. Aqueous systems operate at substantially lower temperatures than molten salts and avoid the synthesis and purification requirements associated with many ionic liquids. However, overall cost-effectiveness cannot be inferred from electrolyte price or operating temperature alone, as it depends on system-specific factors including Faradaic efficiency, CO production rate, energy consumption, catalyst durability, electrolyte recovery, and product-separation requirements. Higher electrolyte or operating costs may therefore be offset by improved catalytic performance or process productivity.

3.1. Electrolyte Environment and CO_2-to-CO Mechanism

Aqueous electrolytes containing dissolved salts such as $KHCO_3$, $NaHCO_3$, or KCl are among the most widely used media for CO_2 reduction. The ionic compounds provide enough ionic conductivity to facilitate ionic charge transport and buffer the solution to maintain a stable pH during the reaction. The choice of cation and anion can also influence CO_2 solubility, reaction selectivity [23,24], and competition with HER [25], making aqueous electrolytes highly versatile for both laboratory and potential industrial applications. However, despite these advantages, aqueous electrolytes face several inherent limitations. The solubility of CO_2 in water is relatively low (~0.034 M), which restricts mass transport and often leads to lower achievable current densities. Additionally, the ready availability of protons in water promotes HER, which competes with CO_2 reduction and can significantly reduce the selectivity toward desired carbon-based products, including CO. Local pH changes during electrolysis can further impact catalyst activity and product distribution, particularly at higher current densities, while high ionic concentrations or prolonged operation can cause salt accumulation or precipitation near the electrode, leading to concentration polarization. Taken together, these factors illustrate that while aqueous electrolytes are practical and widely used for CO production, limitations in CO_2 transport, proton availability, and local reaction conditions can constrain efficiency and selectivity.

The reduction of CO_2 to CO is a proton-coupled electron transfer (PCET) that occurs at the cathode of the electrochemical cell [26,27]. It begins with the adsorption of CO_2 onto an active site of the catalyst, forming an activated carboxyl intermediate upon addition of a proton, which originates from water molecules or hydronium ions in the electrolyte. As represented in Figure 3, this intermediate then undergoes a second proton–electron transfer,

decomposing into CO and H_2O. Finally, the CO molecule desorbs from the catalyst surface, freeing the site for the next reaction cycle. At the anode, water is oxidized to produce O_2, protons, and electrons, which complete the circuit and maintain charge balance in the system.

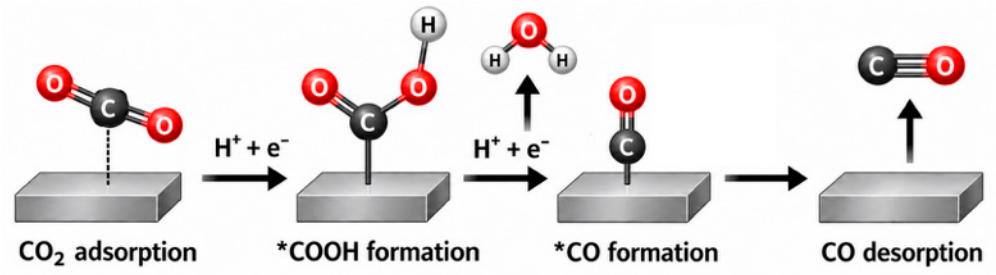


Figure 3. Reaction pathway for the electrochemical reduction of CO_2 to CO. (*) denotes an intermediate adsorbed on the catalyst surface.

The elementary reaction steps of this mechanism are summarized in Table 1.

Table 1. Proposed mechanism for the electrochemical reduction of CO_2 to CO in aqueous media. All elementary reaction steps occur at the cathode unless otherwise indicated; the corresponding anodic oxidation reaction is included for completeness.

Step	Label
$CO_2 + * \rightarrow *CO_2$	Adsorption
$*CO_2 + e^- + H^+ \rightarrow *COOH$	First PCET
$*COOH + e^- + H^+ \rightarrow *CO + H_2O$	Second PCET and CO formation
$*CO \rightarrow CO\ (g) + *$	Desorption
(anode) $2H_2O \rightarrow O_2 + 4H^+ + 4e^-$	Counter-electron reaction/oxygen evolution

(*) denotes an active site or an intermediate adsorbed on the catalyst surface.

Because water participates chemically in supplying protons for the CO_2 reduction reaction, there is an inherent risk of the competing hydrogen evolution reaction. The availability of protons from water or hydronium ions facilitates both CO_2 reduction and HER, and under certain potentials the catalyst may preferentially reduce protons to H_2 rather than converting CO_2 to CO. This competition can significantly decrease the Faradaic efficiency toward CO (FE_{CO}), especially at more negative potentials or on catalysts with poor CO_2-binding affinity.

This competition is thermodynamically justified because, at pH 7, the equilibrium potential for HER is 0 V vs. the reversible hydrogen electrode (RHE), whereas that for CO_2 reduction to CO is approximately −0.12 V vs. RHE, making HER thermodynamically accessible at less negative potentials. Combined with the high proton availability in aqueous electrolytes, HER often dominates when cathodic potentials sufficient for CO_2 activation are applied.

Table 2 shows that the equilibrium potentials for many CO_2 reduction products lie within a few tenths of 0 V vs. RHE, although reaction kinetics—especially for multielectron pathways—make efficient catalysis essential. It also illustrates why selective catalysts are needed to suppress HER and favor CO_2 reduction.

The adsorption–desorption behavior of the catalyst surface is one of the key determinants of product selectivity in the electrochemical CO_2 reduction reaction. First, CO_2 activation requires its adsorption onto an active site, because only the adsorbed $*CO_2$ species can accept electrons and protons to form reactive intermediates such as *COOH, *HCOO, *CHO, or *CO. Catalysts that bind CO_2 too weakly are unable to activate the molecule

effectively, whereas surfaces that bind CO_2 more strongly stabilize specific adsorption geometries, steering the reaction toward distinct reaction intermediates. Second, the binding strength and stabilization of these intermediates dictate which reaction pathways are thermodynamically and kinetically accessible. For example, weak *CO binding on metals such as Au and Ag favors rapid CO desorption, yielding CO as the dominant product, whereas the moderate binding strength of *CO and other intermediates on Cu allows these species to remain on the surface long enough to undergo further PCET or C–C coupling, leading to deeper reductions such as CH_4, CH_3OH, or C_2^+ products.

Table 2. Equilibrium and formal potentials for CO_2 reduction and related reactions at pH 7, expressed vs. RHE.

Reaction	Potential (V vs. RHE, pH = 7)	Product
$CO_2 + 8H^+ + 8e^- \rightarrow CH_4 + 2H_2O$	+0.17	Methane
$CO_2 + 6H^+ + 6e^- \rightarrow CH_3OH + H_2O$	+0.03	Methanol
$2H^+ + 2e^- \rightarrow H_2$	0.00	Hydrogen (HER)
$CO_2 + 4H^+ + 4e^- \rightarrow HCHO + H_2O$	−0.07	Formaldehyde
$CO_2 + 2H^+ + 2e^- \rightarrow CO + H_2O$	−0.12	Carbon monoxide
$CO_2 + 2H^+ + 2e^- \rightarrow HCOOH$	−0.20	Formic acid
$CO_2 + e^- \rightarrow CO_2^{\bullet -}$	−1.49	CO_2 radical anion

Potentials originally expressed vs. NHE were converted to RHE at pH 7 and 25 °C.

In contrast, catalysts that strongly bind hydrogen intermediates tend to favor the hydrogen evolution reaction. Importantly, the competition between CO_2 reduction and hydrogen evolution is not governed by independent surface processes. Cave et al. demonstrated that adsorbed CO intermediates formed during CO_2 reduction can modify hydrogen adsorption on transition-metal surfaces, altering the intrinsic HER activity compared with that measured in CO_2-free environments [28]. Conversely, systems that increase local *H availability can promote further hydrogenation of CO_2-derived intermediates without proportionally increasing HER [29]. These results highlight that catalyst selectivity depends not only on the binding strength of individual intermediates, but also on interactions between co-adsorbed species under operating conditions. Finally, the desorption of reaction products is equally important: products that desorb too rapidly cannot undergo further reduction, while products that desorb too slowly can block active sites, suppressing CO_2 activation and enabling competing reactions. Together, these adsorption, stabilization, and desorption steps define the mechanistic landscape of CO_2 reduction and are central to establishing the selectivity of any electrocatalyst.

3.2. How Nanoparticle Structure Controls the Reaction

Gold and silver represent the classical CO-selective end of the metal-dependent adsorption spectrum [30]. Their surfaces stabilize *COOH sufficiently to enable CO_2 activation while binding *CO weakly enough to favor rapid CO desorption [31]. Copper behaves differently: its stronger interaction with *CO allows the intermediate to remain on the surface and undergo further proton–electron transfer or C–C coupling, enabling deeper reduction products [3,4]. Bismuth provides another contrasting case, preferentially stabilizing *OCHO rather than *COOH and therefore favoring formate formation over CO [32]. These differences illustrate that the elemental identity of the nanoparticle establishes the baseline adsorption energetics from which size, morphology, alloying, and other nanoscale modifications operate.

3.3. Nanoparticle Design Strategies

Once the baseline adsorption behavior is established by metal identity, nanoparticle engineering modifies coordination, electronic structure, and the local reaction environment to shift that baseline selectivity.

For example, the adsorption energetics of Cu can be tuned through alloying with Ni. Because Cu normally retains CO and favors further reduction, shifting Cu-based catalysts toward selective CO production represents a substantial departure from the intrinsic behavior of the metal. Pan et al. demonstrated that precisely controlled Cu–Ni nanocrystals exhibit composition-dependent CO selectivity, with intermediate alloy ratios optimizing the stabilization of the *COOH intermediate while suppressing HER [33]. Yang et al. further showed that tailoring Cu/Ni ratios and particle dispersion modulates the d-band electronic structure, strengthening *COOH formation pathways and enabling high CO output [34].

Beyond alloy composition alone, atomic ordering can further modify catalytic behavior. Ordered AuCu nanoparticles outperform disordered alloys because atomic ordering modifies the electronic structure and optimizes the binding energies of key CO_2 reduction intermediates [35]. The importance of adsorption energetics is further illustrated by bimetallic catalysts such as gold–tin nanoparticles, where tuning the Au/Sn ratio modifies the electronic structure and adsorption properties, enabling control over the selectivity between CO and formate [36].

Particle size and morphology influence catalytic behavior in part by changing the distribution of surface sites with different coordination environments. Early studies of Au nanoparticles demonstrated strong size-dependent effects, although the reported trends were not identical. Zhu et al. found an experimental optimum near 8 nm, achieving an FECO of ~90%, while their theoretical analysis predicted that particles in the 2.7–4 nm range should maximize the density of edge sites favorable for CO formation [37]. Because bulk Au is already highly selective toward CO, the significance of this result lies less in the high FECO itself than in the observed dependence of catalytic behavior on particle size and surface-site distribution. Mistry et al. subsequently observed that decreasing Au nanoparticle size increased overall current density but reduced CO selectivity, as the growing population of low-coordination sites increasingly favored hydrogen evolution [38]. More recently, Sedano Varo et al. identified an experimental CO-selectivity optimum around 3 nm and showed that nanoparticle shape changes concurrently with size. High-resolution microscopy revealed that multiply twinned particles near this optimum contained a high abundance of 8-fold coordinated surface sites associated with enhanced CO formation [39]. These results indicate that apparent particle-size effects reflect changes in the distribution of specific surface structures rather than particle diameter alone.

In contrast to Au nanoparticles, palladium nanoparticles exhibit a volcano-shaped size dependence for the reduction to CO, with optimal performance at approximately 3.7 nm. Gao et al. found that both activity and CO selectivity increased as particle size decreased from 10.3 to 3.7 nm, with the FE_{CO} rising from 5.8% to 91.2% and the current density increasing by approximately 18-fold. However, further decreases in particle size (2.4 nm) led to reduced performance, which was attributed to stronger binding of reaction intermediates and CO, hindering product desorption despite enhanced CO_2 activation at undercoordinated edge and corner sites [40]. Thus, increasing the fraction of undercoordinated sites can enhance CO_2 activation only up to the point at which stronger intermediate and product binding begins to inhibit turnover.

Liu et al. highlighted that triangular Ag nanoplates exhibited higher Faradaic efficiency toward CO than spherical nanoparticles of similar size due to an optimized edge-to-corner atom ratio and preferential exposure of Ag(100) facets [41]. While fewer studies exist

compared with gold, the shape- and facet-dependent selectivity trends underscore the importance of nanostructure design in tuning CO_2 reduction activity on Ag.

Size effects are also metal-dependent. For Cu nanoparticles ranging from 2 to 15 nm, Reske et al. found no analogous optimum; decreasing particle size instead shifted selectivity toward CO and H_2 at the expense of CH_4 and C_2H_4 [42]. Together, the Au, Pd, Ag, and Cu studies show that particle size influences selectivity primarily through the surface structures and adsorption environments it creates rather than through size itself.

Beyond alloying and geometric control, nanoparticle reactivity can also be tuned by modifying the electronic environment of surface metal atoms. Changes in oxidation state, ligand functionalization, and lattice strain represent distinct approaches to alter local charge distribution and the adsorption energies of key CO_2-reduction intermediates, although their effects arise through different physical mechanisms. Low-valent metal states can modify electron density and orbital occupancy at catalytic sites. For instance, Xu et al. demonstrated that low-valent Ni nanoparticles supported on carbon exhibited high selectivity toward CO in aqueous electrolyte, achieving an FE_{CO} of ~98% over a wide potential window (−0.6 to −1.1 V vs. RHE), highlighting the role of valence-state control in CO_2-to-CO selectivity [43]. Ligand functionalization provides a different route to modify the nanoparticle surface. Kim et al. [44] prepared ~5 nm Ag nanoparticles immobilized on carbon using cysteamine as an anchoring ligand, obtaining a fourfold increase in FE_{CO} at −0.75 V vs. RHE relative to polycrystalline Ag foil. Density functional theory (DFT) calculations indicated that interactions between the Ag nanoparticles and cysteamine modified the surface affinity for COOH relative to CO, contributing to the lower overpotential and improved CO selectivity.

Lattice strain provides a different route to electronic modification by changing metal–metal spacing and orbital overlap, thereby altering the electronic states that govern adsorbate binding. Zhang et al. used laser ablation in liquid, a surfactant-free physical synthesis method capable of producing high-purity nanoparticles, to introduce compressive strain into Au nanoparticles, shifting the Au d-band center and enhancing *COOH adsorption. The strained Au nanoparticles reached an FE_{CO} of 97% at −0.9 V vs. RHE, illustrating how lattice distortion can modify intermediate binding and selectivity [45].

Surface ligands can likewise redistribute charge at metal sites, but their influence extends beyond electronic effects by modifying steric accessibility, local solvation, water and proton availability, and reactant transport near the catalyst interface. Ghosh et al. reported cyclic(alkyl)(amino)carbene-stabilized Au nanoparticles with an FECO of ~94% at pH 6.3, compared with ~60% for oleylamine-capped Au nanoparticles at the same potential. The carbene-stabilized catalyst also exhibited faster CO_2-reduction kinetics, demonstrating that ligand identity can substantially modify the catalytic behavior of otherwise similar Au nanoparticles [46]. Souza et al. functionalized small Au nanoparticles with dibenzyldithiocarbamate ligands, achieving an FECO of ~100% at −0.8 V in aqueous $KHCO_3$. Compared with citrate-capped Au nanoparticles, the functionalized catalyst showed higher faradaic current and a greater CO/H_2 ratio [47]. Strong ligand binding also suppressed agglomeration, while the hydrophobic dibenzyl groups enhanced CO_2 access and inhibited water reduction.

Spatial confinement of metallic nanoparticles within carbon coatings, nanotubes, or porous conductive frameworks can provide two complementary functions: stabilization of the metallic phase and regulation of the local reaction environment. Carbon layers can mediate contact between the metal surface and the electrolyte while influencing reactant access, intermediate stabilization, and local proton availability. Jia et al. demonstrated the magnitude of this effect with carbon-coated Ni nanoparticles supported on N-doped carbon. Whereas previously reported supported Ni nanoparticles typically exhibited an FECO below 25% and were dominated by hydrogen evolution, the confined catalyst reached an FECO

of ~94% and a CO partial current density of 22.7 mA cm^{-2} [48]. Control Ni nanoparticles supported on carbon without N doping showed poor CO_2-reduction activity, indicating that the carbon coating and support chemistry were essential to redirecting Ni toward CO formation. The carbon coating and N-doped support stabilized *COOH without substantially hindering *CO desorption, thereby favoring CO formation over hydrogen evolution. Ni nanoparticles confined within N-doped carbon nanotubes extended this strategy to acidic conditions, where HER and catalyst corrosion present particularly severe challenges. The carbon shell protected the Ni nanoparticles from etching, promoted CO_2 adsorption, and regulated local pH, enabling near-unity CO selectivity over acidic, neutral, and alkaline conditions. In acidic electrolyte, the catalyst reached an FECO of 97.4% at −1.44 V, while at −1.74 V the current density reached ~288 mA cm^{-2} with a TOF of ~11,000 h^{-1} [49].

Encapsulation can also modify the electronic properties of catalytically active surface sites through subsurface or core–shell interactions. Cheng et al. embedded Fe_2N nanoparticles within Fe,N-codoped carbon shells. At −0.53 V vs. RHE, the resulting catalyst reached an FECO of ~95% and a CO partial current density of ~4.47 mA cm^{-2}, compared with 73% and ~1.12 mA cm^{-2}, respectively, for the corresponding Fe–N/CNF catalyst without the Fe_2N core. DFT calculations indicated that the encapsulated Fe_2N core facilitates CO desorption from Fe–N_4 sites in the surrounding carbon shell, directly linking the performance enhancement to electronic coupling between the nanoparticle core and the active surface [50].

Confinement can also facilitate electronic communication between metallic nanoparticles, conductive supports, and neighboring active sites. Ren et al. exploited this effect in a cooperative Ni single-atom-on-nanoparticle catalyst, in which confined Ni nanoparticles donated electrons to Ni(I)–N–C sites through a carbon-nanotube network. The coupled catalyst reached a CO partial current density of ~346 mA cm^{-2} at −0.50 V vs. RHE, whereas the Ni single-atom catalyst without the nanoparticle component reached a maximum of ~263 mA cm^{-2} only at −0.65 V. The improvement was attributed to electron donation from the nanoparticles, which enhanced *COOH adsorption at the Ni single-atom sites [51].

Figure 4 summarizes the principal nanoparticle design strategies discussed above and their effects on surface properties, intermediate binding, and catalytic performance.

At the limit of nanoscale structural control, atomically precise metal clusters provide well-defined active-site environments that can help isolate structure–activity relationships that are difficult to resolve in conventional nanoparticles. One important route to activating these clusters is ligand-shell modification: removal of protective ligands from gold clusters such as Au_{25}, Au_{38}, Au_{144}, and Au_{28} can expose undercoordinated Au sites associated with enhanced CO_2-to-CO activity [52,53]. Beyond ligand removal, targeted electronic modifications provide additional control. Single-atom modification of Au_8 clusters can alter the electronic structure and stabilize *COOH intermediates [54], while hydride-bridged $Au_{22}H_3$ clusters demonstrate that incorporated atomic hydrogen can also modulate catalytic reactivity [55]. Multimetallic Au–Ag–Cu clusters further show how elemental composition can redirect selectivity between CO and formate by altering intermediate-binding energetics [56]. Atomically defined clusters therefore provide platforms for isolating active-site and electronic effects that are difficult to resolve in conventional nanoparticles.

Alloying, coordination control, electronic modification, surface functionalization, and confinement can therefore reshape intermediate binding and the local reaction environment. Their effects are often coupled, however, making it essential to distinguish changes in intrinsic surface reactivity from improvements arising from stabilization or transport.

Representative examples of these nanoparticle design strategies and their corresponding catalytic performance are summarized in Table 3.

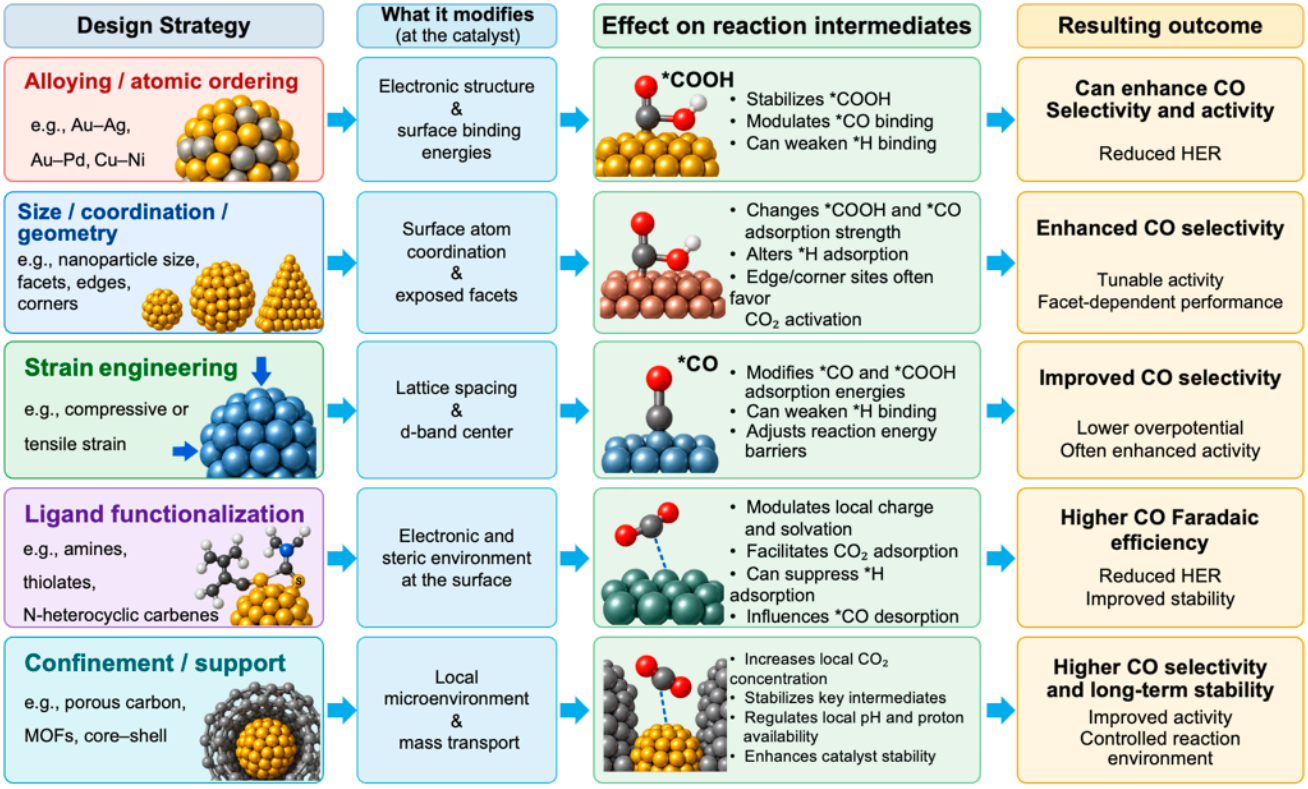


Figure 4. Nanoparticle design strategies for CO_2-to-CO electrocatalysis in aqueous electrolytes. Alloying, size and geometry control, strain engineering, ligand functionalization, and support or confinement modify nanoparticle electronic structure, surface coordination, and the local reaction environment, thereby influencing intermediate binding, CO selectivity, activity, and stability. (*) denotes an intermediate adsorbed on the catalyst surface.

Table 3. Selected representative examples of metallic nanoparticle catalysts for CO_2 electroreduction to CO in aqueous electrolytes, highlighting their performance metrics and key catalyst design features.

Metal/ Catalyst	Electrolyte	Potential (V vs. RHE)	FE_{CO} (%)	j_{CO} (mA cm^{-2})	Key Design Feature/Notes	Ref.
Au	0.5 M $KHCO_3$	−0.67	~90	~2–3	Size tuning; ~8 nm gives optimal CO selectivity through favorable surface-site distribution	[37]
	0.1 M $KHCO_3$	−1.22	45	~50	Size-dependent activity; smaller particles increase activity but increasingly favor HER	[38]
	0.1 M $KHCO_3$	−0.4 to −0.8	60	~12	Coupled size–shape effect; ~3 nm twinned particles rich in low-coordination sites favor CO	[39]
	0.1 M $KHCO_3$	−0.9	97	24.9	Compressive strain strengthens COOH adsorption through electronic-structure modification	[45]
	0.5 M $KHCO_3$	−0.7	~94	10	Carbene ligands tune Au electronic structure and promote *CO selectivity	[46]
	0.1 M $KHCO_3$	−0.8	~100	8	Ligand functionalization stabilizes nanoparticles, enhances CO_2 access, and suppresses HER	[47]
	1 M $KHCO_3$	−0.85	>70	~36	Uniform low-loading on gas-diffusion electrode improves catalyst use; mass activity of 1882 A g^{-1}.	[57]

Table 3. *Cont.*

Metal/ Catalyst	Electrolyte	Potential (V vs. RHE)	FE_{CO} (%)	j_{CO} (mA cm^{-2})	Key Design Feature/Notes	Ref.
Ag	0.1 M $KHCO_3$	−0.746	96.8	1.2	Shape/facet control increases favorable edge sites and Ag(100) exposure	[41]
	0.5 M $KHCO_3$	−0.75	79.2	1.00	Cysteamine functionalization modifies *COOH/*CO binding and lowers overpotential	[44]
Pd	0.1 M $KHCO_3$	−0.89	91.2	4–6	Volcano-type size effect; ~3.7 nm balances CO_2 activation and *CO desorption	[40]
Cu	0.1 M $KHCO_3$	−1.1	~20	10–50	Decreasing particle size shifts selectivity toward CO and H_2 over deeper-reduction products	[42]
AuCu	0.1 M $KHCO_3$	−0.5 to −0.9	60–95	5–20	Atomic ordering modifies electronic structure and optimizes intermediate binding	[35]
Au–Sn bimetal	0.1 M $NaHCO_3$	−0.7	45–85	3–12	Au/Sn composition tunes adsorption energetics and CO/formate selectivity	[36]
Ni	0.1 M $KHCO_3$	−0.8	98	7	Valence-state control; low-valent Ni favors selective CO formation	[43]
	0.5 M $KHCO_3$	−1.1	~94	22.7	C coating/N-doped support stabilizes *COOH while maintaining favorable *CO desorption	[48]
	0.5 M $KHCO_3$ & acidic media	−1.44	97.4	–	Nanoconfinement stabilizes Ni, promotes CO_2 adsorption, and regulates the local pH	[49]
	0.5 M $KHCO_3$	−0.5	98	346	Nanoparticle-to-single-atom electronic coupling enhances COOH adsorption and CO selectivity	[51]
Cu-Ni	0.1 M $KHCO_3$ (pH 6.8)	−0.6	99.7	4	CuNi alloying with N-doped carbon tunes electronic structure and intermediate binding	[34]
	3 M KCl (pH 4.25, CO_2-saturated)	−1.0	>95	>399	Cu/Ni ratio control optimizes *COOH stabilization while suppressing HER	[33]

(*) denotes an intermediate adsorbed on the catalyst surface.

3.4. Transport, Electrode Architecture, and Catalyst Stability

Conventional aqueous electrodes, such as planar or nanoparticle-modified electrodes, are constrained by the low solubility of CO_2, which limits the supply of reactant to the active sites and results in much lower current densities, typically too low for industrial applications, even when the catalysts themselves are highly active and selective. In contrast, gas-diffusion electrodes can achieve very high current densities for CO_2-to-CO conversion [58] by delivering CO_2 directly to the catalyst through a three-phase interface, alleviating mass-transport limitations. For example, homogeneous deposition of Au nanoparticles on gas-diffusion electrodes in 1 M aqueous $KHCO_3$ enabled a very high CO mass activity of 1882 A g^{-1} at −0.85 V, highlighting the potential for high-rate CO production in aqueous media [57].

Extended operation has been demonstrated in some aqueous nanoparticle-based systems. Li et al. maintained continuous carbonate electrolysis for 145 h using Ag nanoparticles deposited on an Ag-supported electrode, demonstrating substantial operational durability under flow conditions [59]. However, the system was designed for syngas production rather than highly selective CO formation, illustrating that long operating times do not necessarily correspond to sustained high CO selectivity.

Operational durability alone does not establish structural stability of the catalyst. High initial activity and selectivity do not necessarily translate into sustained performance. Long-term catalyst stability remains less systematically characterized than initial activity and selectivity in CO_2 electroreduction. When directly examined, metallic catalysts have been shown to undergo substantial morphological evolution under CO_2-reduction conditions. For example, identical-location transmission electron microscopy measurements of Ag nanoparticles revealed fragmentation followed by particle growth during electrolysis, accompanied by declining CO selectivity [60]. More recently, Wang et al. showed that incorporating Ni into Ag nanoparticles suppresses surface reconstruction during CO_2 electroreduction, thereby improving catalytic stability relative to pure Ag. The Ag–5%Ni catalyst maintained FE_{CO} above 95% over current densities from 40 to 180 mA cm^{-2}, illustrating that nanoparticle composition can influence not only activity and selectivity but also structural durability [61]. Using a different analytical approach, online inductively coupled plasma mass spectrometry measurements of Au and Cu electrodes detected catalyst degradation through nanoparticle detachment under CO_2-reduction conditions, even when dissolution into soluble metal ions remained limited [62]. Such observations demonstrate that the catalyst structure present during operation may differ from the initially synthesized material and highlight the need to evaluate structural evolution alongside conventional stability measurements. These observations also highlight the importance of in situ and operando characterization for identifying catalyst states that may not be captured by post-reaction analysis. For example, Mistry et al. combined transmission electron microscopy and operando X-ray absorption spectroscopy with quasi-in situ X-ray photoelectron spectroscopy on plasma-activated Ag, showing that oxygen species persisted within the catalyst while the surface was metallic under CO_2-reduction conditions [63]. More broadly, operando X-ray absorption, Raman and infrared spectroscopies, and advanced microscopy can help resolve transient changes in oxidation state, surface structure, and adsorbed intermediates under working conditions [64–66].

Electrode architecture also complicates comparisons among reported catalysts. Improvements in geometric current density may arise from changes in catalyst loading [67] or electrode architecture and CO_2 transport [68] rather than from changes in intrinsic surface activity. Accordingly, geometric current density, mass activity, ECSA-normalized activity, and stability measurements provide complementary information and should not be interpreted interchangeably.

3.5. Design Principles and Limitations

Overall, aqueous electrolytes provide the most established framework for understanding nanoparticle-catalyzed CO_2 reduction to CO. Metal identity defines the baseline adsorption energetics, while composition, particle size, surface coordination, electronic structure, ligands, and support interactions provide additional control over intermediate binding and selectivity. Effective CO-selective catalysts generally balance *COOH stabilization with sufficiently weak *CO binding and suppression of competing hydrogen evolution. Nevertheless, performance remains strongly influenced by CO_2 mass transport, local pH, electrode architecture, and catalyst stability. These coupled effects complicate direct comparisons of intrinsic catalyst activity. However, the extensive mechanistic understanding and broad catalyst literature available for aqueous CO_2 electroreduction make aqueous systems a useful reference for examining how different electrolyte environments modify nanoparticle behavior.

4. Ionic-Liquid Electrolytes

Ionic liquids (ILs) are salts with low melting points that have emerged as distinctive electrolytes for electrochemical CO_2 reduction because of their unusual physicochemical

properties. Depending on their composition, ILs can exhibit high CO_2 solubility, wide electrochemical stability windows, negligible vapor pressure, and highly tunable ionic environments [69–72]. These characteristics provide additional control over interfacial reactions and make ILs compatible with a broad range of electrode materials, including metallic nanoparticles. Early conceptual frameworks, including that summarized by Dupont in 2019, emphasized the ability of ILs to interact strongly with CO_2, modify proton availability and hydrogen evolution, and stabilize activated CO_2-derived intermediates through specific ionic and interfacial interactions [73].

4.1. Interfacial Structure, CO_2 Activation, and Proton Availability

In aqueous electrolytes, the one-electron reduction of CO_2 to the radical anion $CO_2^{\bullet-}$ is thermodynamically accessible but kinetically difficult because the reduced species is highly reactive and readily quenched. As a result, CO_2 reduction generally proceeds through surface-bound intermediates such as $*CO_2$ and *COOH. In ionic liquids, particularly imidazolium-based systems, the organized interfacial environment and electric double layer formed at the catalyst–electrolyte interface can stabilize reduced CO_2 species [74]. This stabilization lowers the energetic penalty associated with the initial electron-transfer step and can make $CO_2^{\bullet-}$ or related ion-paired or surface-associated species more persistent at the interface.

Following the initial electron transfer (activation), $CO_2^{\bullet-}$ can interact with the ionic-liquid cation to form a stabilized ion-paired species before adsorption at the catalyst surface. Subsequent protonation produces the *COOH intermediate, followed by a PCET step that forms *CO and water. The proposed sequence is summarized in Table 4.

Table 4. Proposed mechanism for the electrochemical reduction of CO_2 to CO in ionic-liquid media. The first two steps illustrate CO_2 activation and stabilization by the ionic-liquid electrolyte prior to adsorption at the catalyst surface; the remaining elementary steps occur at the cathode.

Step	Label
$CO_2 + e^- \rightarrow CO_2^{\bullet-}$	Activation
$CO_2^{\bullet-} + [\text{Cation}] \rightleftharpoons [\text{Cation}\cdots CO_2^{\bullet-}]$	Cation stabilization
$[\text{Cation}\cdots CO_2^{\bullet-}] + * \rightarrow *CO_2^- + [\text{Cation}]$	Surface Adsorption
$*CO_2^- + H^+ \rightarrow *COOH$	Protonation/carboxyl formation
$*COOH + H^+ + e^- \rightarrow *CO + H_2O$	Second PCET and CO formation
$*CO \rightarrow CO + *$	Desorption

(*) denotes an active site or an intermediate adsorbed on the catalyst surface.

The identity of the proton donor depends strongly on the presence of protic species in the electrolyte. In systems containing trace or added water, proton transfer is generally attributed to water or hydronium-derived species, which participate in PCET steps leading to *COOH and *CO intermediates. In this regime, the ionic liquid primarily modifies the interfacial environment and local proton availability. Under nominally anhydrous conditions, several alternative proton sources have been proposed. Although imidazolium cations, such as 1-butyl-3-methylimidazolium ($[BMIM]^+$) and 1-ethyl-3-methylimidazolium ($[EMIM]^+$), are not classical Brønsted acids, their ring C–H groups have been suggested to participate in proton transfer under electrochemical polarization, although the identity of the active site (C2 versus C4/C5) remains debated [75–77]. Alternatively, the imidazolium cation may act as a transient hydrogen-bond donor or proton shuttle rather than a stoichiometric proton donor [78]. The extent to which these pathways contribute relative to residual protic impurities remains dependent on the structure of the specific ionic liquid, electrode material, and operating conditions.

Complementary work by Sun et al. proposed a reaction pathway in which imidazolium-based ionic liquids stabilize reduced CO_2-derived intermediates at the electrode–electrolyte interface, even in the presence of water [79]. A schematic representation of the possible involvement of the ionic-liquid environment in CO_2 activation and subsequent proton-transfer steps is presented in Figure 5.

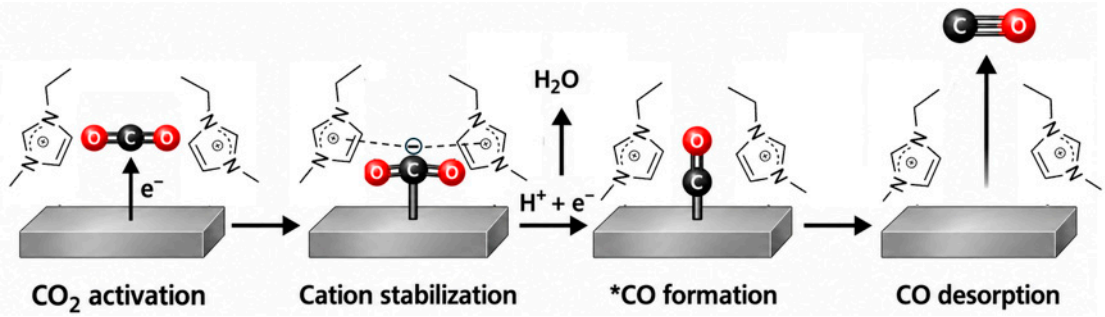


Figure 5. Proposed reaction pathway for the electrochemical reduction of CO_2 to CO in the presence of [EMIM], highlighting the role of the ionic-liquid environment in stabilizing CO_2-derived intermediates at the electrode–electrolyte interface. Scheme based on the mechanistic concepts discussed in Refs. [74–79]. (*) denotes an intermediate adsorbed on the catalyst surface.

Mechanistic studies illustrate this complexity. Wang et al., using sum-frequency generation spectroscopy and DFT, proposed direct participation of $[EMIM]^+$ through formation of an $[EMIM–COOH]^-$ intermediate, with water acting as a co-catalyst when present [75]. Although such studies support an active role of the ionic liquid in CO_2 activation and proton transfer, the exact nature of the activated species—free $CO_2^{\bullet-}$, an ion-paired species, or a surface-bound intermediate—remains system-dependent.

4.2. Electric-Double-Layer, Ion–Surface, and Local-Field Effects

Unlike in aqueous electrolytes, where $CO_2^{\bullet-}$ is highly unstable, ionic liquids can lower the energetic penalty associated with the initial electron-transfer step by stabilizing charged CO_2-derived species within the interfacial region. This stabilization can reduce the activation barrier for CO_2 reduction and contribute to lower overpotentials [17] and enhanced CO selectivity. This effect is illustrated schematically in Figure 6, which compares the free-energy profiles for CO_2 reduction in aqueous/acetonitrile, and imidazolium-based ionic-liquid media.

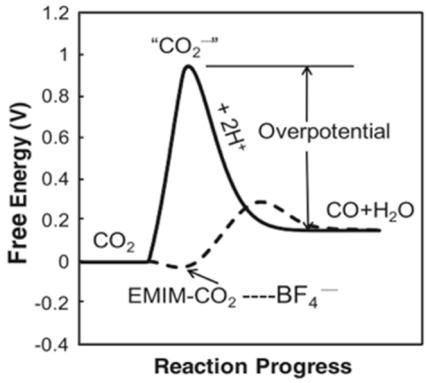


Figure 6. Free-energy profile for CO_2 electroreduction to CO in water/acetonitrile and EMIM-BF_4 electrolytes. The ionic-liquid environment lowers the activation barrier, facilitating CO formation and reducing the required overpotential. Reproduced with permission from Rosen et al., Science Science, published by AAAS, 2011 [17].

Further insight into the role of ionic liquids has been provided by studies of the electrode interface. Lau et al. showed that imidazolium cations can function as co-catalytic promoters rather than inert electrolyte components by stabilizing CO_2-derived intermediates through local electric field effects and specific ion–intermediate interactions on Ag electrodes [76]. Similarly, Liu et al. showed that CO_2 reduction kinetics depend strongly on ionic screening, with maximum activity occurring at intermediate EMIM-BF_4 concentrations where ionic correlations generate strongly localized electric fields that stabilize reaction intermediates [80]. At higher concentrations of the ionic liquid, carbonate passivation begins to limit performance. These findings demonstrate that the catalytic activity of ionic-liquid electrolytes is intrinsically linked to the structure of the electric double layer and the local interfacial environment.

Ju et al. demonstrated how the electrolyte environment can enhance CO_2 reduction on an already CO-selective Ag surface using a mixed ionic-liquid/propylene carbonate electrolyte [81]. In [BMIM][BF_4]/PC, the current density reached 8.2 mA cm^{-2} at −1.90 V vs. Fc/Fc^+, approximately three times that obtained in [Bu_4N][BF_4]/PC under the same conditions, while CO selectivity increased and hydrogen evolution was suppressed. Electrochemical measurements indicated that adsorbed imidazolium cations stabilize $CO_2^{\bullet-}$-like intermediates at the Ag surface, facilitating the initial electron-transfer step. The low proton availability of the propylene carbonate-based medium further disfavors hydrogen evolution.

Rosen and co-workers examined the complementary effect of increasing water content in EMIM-BF_4 [82]. Using Ag nanoparticle-based electrodes, they found that adding water increased CO formation while H_2 production remained low over a broad composition range, up to approximately 90 mol% water. The enhancement was attributed to hydrolysis of BF_4^-, which provides protons that accelerate CO_2 reduction, while the ionic-liquid environment continues to suppress competing hydrogen evolution. This study demonstrates that proton availability in ionic-liquid media can be tuned over a wide range without necessarily sacrificing CO selectivity.

Ion organization, ionic screening, and local electric fields therefore influence CO_2 activation and intermediate stabilization, with their effects depending on the catalyst surface.

4.3. Nanoparticle–Ionic-Liquid Interactions and Representative Catalyst Strategies

On metallic nanoparticles, particle composition, surface coordination, facet structure, and curvature may alter ion adsorption and the organization of the electric double layer, potentially changing the extent to which the ionic liquid modifies reaction energetics.

Zhang et al. [83] demonstrated that the surface condition of bismuth nanoparticles can be more important than particle size in determining CO_2-to-CO selectivity. This behavior contrasts strongly with the formate selectivity generally associated with Bi in aqueous media [32]. In acetonitrile containing [BMIM][OTf] (BMIM triflate), activated bismuth nanoparticles reached an FE_{CO} of 96.1% after removal of residual oxides and surfactants. The chemical state and accessibility of the nanoparticle surface therefore influence intermediate binding and selectivity in ionic-liquid-containing media. Complementing these experimental observations, Zhou et al. [84] used DFT to investigate different Bi oxidation states and surface structures, predicting that metallic bismuth (Bi^0) favors CO formation over formate, whereas Bi_2O_3 preferentially promotes formate formation. Together, these studies indicate that apparent nanoparticle-size effects can be strongly influenced by surface oxidation state and surface condition.

The importance of exposed surface structure is also evident in nanostructured Ag catalysts. Because Ag is intrinsically CO-selective, the significance of nanostructuring in this case lies more in controlling interfacial structure and sustaining high-rate CO production than in creating CO selectivity itself. Zhang et al. [85] reported Ag(111)-dominant

nanofoams in [BMIM][BF_4] with FE_{CO} values above 95% over −1.9 to −2.4 V vs. Ag/Ag^+ and a CO current density of approximately 125 mA cm^{-2}. At −2.4 V, this j_{CO} was about 62% higher than that of an Ag(110)-dominant Ag electrode under the same conditions (77.35 mA cm^{-2}), demonstrating that the advantage of the nanofoam was not simply high CO selectivity but enhanced CO production rate associated with its exposed surface structure. DFT calculations indicated preferential interaction of the ionic-liquid environment with Ag(111), contributing to stabilization of reaction intermediates. At an even more structurally defined scale, Lin et al. [86] examined an atomically precise $AuAg_{26}$ nanocluster with an open-shell structure that exposes four triangular facets of the metal kernel. The catalyst reached an FECO of 98.4% at −0.97 V, compared with approximately 55% for Ag_{25} and 4% for Au_{21} nanoclusters under comparable conditions. In situ infrared measurements and DFT calculations associated this enhanced selectivity with the exposed sites of the open-shell structure, which favor *COOH formation, consistent with the importance of surface coordination and atomically defined active-site environments previously observed for nanoclusters in aqueous media [52–56].

Particle size provides another means of tuning the nanoparticle–ionic-liquid interface. Salehi-Khojin et al. [87] examined Ag nanoparticles ranging from approximately 1 to 200 nm in EMIM-BF_4 and observed a pronounced size dependence, with maximum activity near 5 nm. The CO_2 electrolysis rate normalized to surface area was approximately ten times that of bulk Ag, whereas activity decreased again for particles near 1 nm, producing a volcano-type dependence attributed to changes in intermediate binding with particle size. A related effect was reported by Zhu et al. [37] for Au nanoparticles. Eight-nanometer Au nanoparticles embedded in BMIM-PF_6 reached an FE_{CO} of up to 97% and approximately 3 A g^{-1} at −0.52 V, outperforming the corresponding Au nanoparticle catalyst without the ionic-liquid environment. The enhancement was attributed to stabilization of *COOH, illustrating that nanoparticle structure and ionic-liquid-mediated intermediate stabilization can act cooperatively rather than independently.

More deliberate control of the nanoparticle–electrolyte interface can be achieved through surface functionalization. Li et al. [88] modified Ag nanoparticles with 3-mercapto-1,2,4-triazole and employed them in a mixed electrolyte containing [BMIM][PF_6], acetonitrile, and water. The functionalized catalyst reached an FE_{CO} of 99.2% and a CO current density of 85 mA cm^{-2} at −2.3 V vs. Ag/Ag^+, with approximately 2.5 times the current density of Ag powder. The ligand enhanced CO_2 adsorption and modified the energetics of *COOH formation. This example shows that ligand functionalization and ionic-liquid composition can provide complementary control over the same interfacial reaction environment.

Nanoparticle effects in ionic-liquid media cannot be described by particle size alone. Surface condition, crystallographic structure, coordination environment, particle size, and ligand functionalization all influence how the metallic surface interacts with the ionic-liquid environment and how CO_2-derived intermediates are stabilized. The resulting catalytic behavior therefore reflects a coupled catalyst–electrolyte interface rather than independent contributions from the nanoparticle and electrolyte.

4.4. Transport, Stability, Cost, and Practical Limitations

A major limitation of ionic liquids is their high viscosity, which can be orders of magnitude greater than that of aqueous electrolytes. This significantly reduces diffusion coefficients of CO_2 and reaction intermediates, making mass transport a rate-limiting factor in many systems. As a result, in diffusion-limited regimes, improvements in catalyst activity may not translate into higher current densities. To partially address this limitation and decouple kinetic effects from transport constraints, rotating disk electrode configurations are often employed to control convection and better isolate intrinsic catalytic behavior.

Rudnev et al. [89] compared nanostructured Ag foam with planar Ag foil in a [BMIM][BF_4]-based electrolyte. The porous Ag foam shifted the onset of CO_2 reduction by approximately 220 mV toward less negative potentials; however, at higher reaction rates the current became mass-transport-limited, such that the substantially larger surface area of the foam did not translate proportionally into higher current density. Addition of water, with an optimum mole fraction of approximately 20%, further improved performance and enabled FECO values above 94%, reflecting the combined influence of electrolyte viscosity, ionic conductivity, and proton availability. A more direct demonstration of transport effects was provided by Vedharathinam et al. [90], who deposited Ag nanoflowers on porous aluminum foam in [EMIM][BF_4]/water and varied the electrolyte flow through the electrode. At 100 mL min^{-1}, the CO partial current density reached approximately 36.6 mA cm^{-2}, representing about a 70-fold increase relative to the no-flow condition, while FECO increased from approximately 10% to 75%. Together, these studies show that increasing catalyst surface area alone is insufficient when CO_2 transport is limiting, whereas enhanced convective transport through porous electrodes can substantially increase the achievable CO production rate.

Beyond mass transport, practical implementation of ionic-liquid electrolytes is complicated by synthesis and purification requirements, sensitivity to electrolyte composition, and environmental and economic considerations. Water content can strongly alter proton availability and catalytic selectivity in ionic-liquid electrolytes, as demonstrated by Rosen et al. [82] and Rudnev et al. [89]. Consequently, careful control of electrolyte composition is important when comparing catalytic performance across ionic-liquid systems. Although the relatively high cost of some ionic liquids is frequently cited as a limitation [91], technoeconomic analyses suggest that electrolyte cost itself may represent only a small fraction of the overall cost of CO production if the ionic liquid can be efficiently recovered and reused [71]. Environmental considerations also remain important: negligible vapor pressure does not necessarily imply low environmental impact, and the toxicity and biodegradability of ionic liquids vary substantially with cation and anion structure [92,93].

Progress toward larger-scale operation has nevertheless been demonstrated. Yuan et al. developed an ionic-liquid-based flow electrolyzer with an electrode area of 495 cm^2, achieving a total current of 6.32 A and an FE_{CO} of 83.9% under optimized conditions [94]. The 495 cm^2 electrolyzer demonstrates operation beyond small laboratory cells, while also highlighting the importance of electrolyte circulation, mass transport, water management, and electrolyte recovery when moving toward larger electrode areas.

Long-term stability remains considerably less investigated than initial activity and selectivity. Rosen et al. demonstrated sustained CO production for at least 7 h with FE_{CO} values above 96% in an early ionic-liquid-mediated system [17], while Yuan et al. later reported approximately 10 h of continuous operation under larger-area flow-cell conditions [94]. By comparison, substantially longer operation has been demonstrated in aqueous nanoparticle-based systems, including 145 h of continuous carbonate electrolysis using Ag nanoparticles, although that system was operated for syngas rather than highly selective CO production [59]. Other studies have shown that ionic-liquid composition itself can influence chemical stability and that changes in electrolyte composition may occur during extended electrolysis [95,96]. Although these results demonstrate short-term operational stability, the reported timescales for IL-based systems remain far below those required for practical implementation. Long-duration electrolysis combined with post-reaction characterization of both the catalyst and electrolyte is therefore needed to determine whether catalyst restructuring, electrolyte degradation, or changes in the catalyst–electrolyte interface ultimately limit sustained performance.

The principal nanoparticle and interfacial design strategies discussed in Sections 4.1–4.4 are summarized in Figure 7.

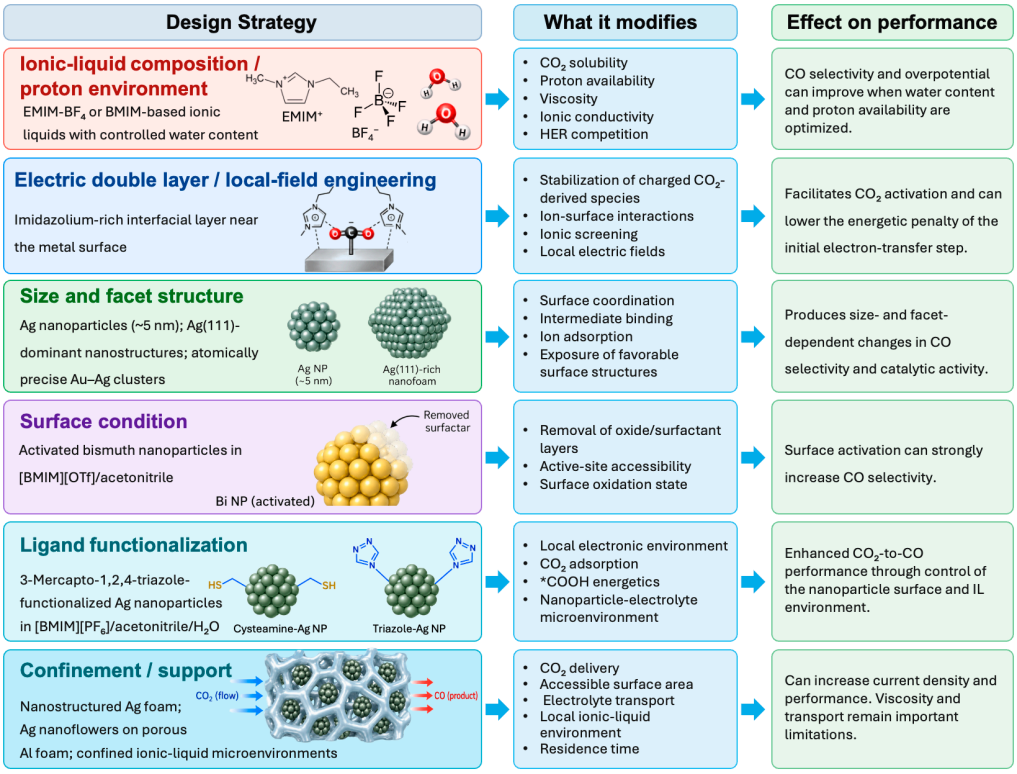


Figure 7. Nanoparticle and interfacial design strategies for CO_2-to-CO electrocatalysis in ionic-liquid media. Ionic-liquid composition, interfacial electric-double-layer effects, nanoparticle size and facet structure, surface condition, ligand functionalization, and porous electrode architecture influence CO_2 activation, intermediate stabilization, proton availability, and mass transport. Their combined effects determine CO selectivity, activity, and practical performance. (*) denotes an intermediate adsorbed on the catalyst surface.

4.5. Design Principles and Knowledge Gaps

Nanoparticle-based CO_2-to-CO electrocatalysis in ionic-liquid media requires simultaneous control of the catalyst surface and the surrounding electrolyte environment. Particle composition, size, surface coordination, oxidation state, ligands, and exposed facets determine the intrinsic adsorption properties of the metallic surface, while the ionic liquid modifies CO_2 activation, intermediate stabilization, proton availability, and the structure of the interfacial region. Consequently, catalyst and electrolyte properties should be considered as coupled design variables rather than optimized independently. The influence of catalyst identity is further illustrated by studies of Ru nanoparticles in ionic-liquid media, where CO_2 conversion predominantly yields CH_4, with CO appearing mainly as an intermediate or minor product [97,98]. Although these systems involve catalytic hydrogenation rather than electrochemical CO_2 reduction, they reinforce the broader point that ionic liquids modify the local reaction environment without independently determining product selectivity.

Nanoconfinement provides one emerging strategy for controlling this interfacial environment. Sun et al. [99] showed that nanoconfined ionic liquids surrounding atomically dispersed Ni–N–C sites can sustain efficient CO_2 reduction even at low CO_2 concentrations. Although this catalyst lies outside the strict class of metallic nanoparticles, the study demonstrates how localized ionic-liquid domains near active sites can regulate CO_2 availability and proton-transfer conditions. Related effects have been observed for metallic nanoparticles, where incorporation of Au nanoparticles into an ionic-liquid-containing microenvironment

enhanced CO selectivity and reduced the required overpotential [37]. These studies suggest that controlling the spatial distribution of the ionic liquid around metallic surfaces may be as important as controlling nanoparticle structure itself.

5. Molten Salt Electrolytes

CO_2 electroreduction in molten salts differs fundamentally from aqueous and ionic-liquid systems because it occurs in an anhydrous, high-temperature ionic environment. Molten salts generally exhibit high ionic conductivity, broad electrochemical and thermal stability, and minimal competition from hydrogen evolution due to the absence of water [100]. Their high-temperature chemistry also changes the form in which CO_2 is present and reduced, making the identity of the electroactive species strongly dependent on electrolyte composition.

5.1. Electrolyte Chemistry and Identity of the Electroactive Species

Operating typically at several hundred degrees Celsius, molten salts provide an anhydrous, highly ionic reaction environment in which CO_2 reduction differs fundamentally from the proton-coupled pathways characteristic of aqueous systems. The mechanistic discussion below focuses primarily on carbonate and carbonate-containing melts, which constitute the best-established systems for selective CO production and for which carbonate–oxide equilibria provide a defined framework for interpreting the cathodic reaction. In these media, CO_2 is coupled to carbonate formation through the equilibrium $CO_2 + O^{2-} \rightleftharpoons CO_3^{2-}$. For the two-electron pathway to CO, reduction generates CO and O^{2-} at the cathode [101]. Chloride-based melts can also support CO_2 conversion, but may involve additional pathways, including in situ carbonate formation or reactions involving electrochemically generated metal species.

The rapid interconversion among dissolved CO_2, O^{2-}, and CO_3^{2-} complicates identification of the actual electroactive species. Incoming CO_2 can be incorporated into the melt as carbonate rather than remaining solely as molecularly dissolved CO_2, so the electrolyte itself acts as a reactive carbon reservoir. Consequently, two general mechanistic descriptions can be considered: reduction initiated from molecular CO_2 and reduction initiated directly from carbonate species.

A molecular CO_2 pathway can be proposed by analogy with low-temperature CO_2 electroreduction (Table 5). However, the formation of surface-bound reduced CO_2 species such as $*CO_2^{\bullet-}$ or $*CO_2^{2-}$ under molten salt conditions has not been directly established and should therefore be regarded as a conceptual mechanistic framework rather than a confirmed sequence.

Alternatively, carbonate ions may participate directly in the cathodic reaction. In this framework, electron transfer is coupled to progressive oxygen removal from adsorbed carbonate-derived species, ultimately producing CO and oxide ions (Table 6). This description is consistent with the dominant carbonate chemistry of the melt but, as with the molecular pathway, the identities of individual surface intermediates remain uncertain.

For lithium carbonate electrolytes, the net cell chemistry can be represented as:

$$Li_2CO_3(l) \rightarrow Li_2O(l) + CO(g) + ½\,O_2(g)$$

This carbonate-mediated interpretation is consistent with Gao et al.'s observation of high oxide-ion concentrations near the cathode [102].

Thus, irrespective of the detailed elementary pathway, oxide-ion formation and carbonate–oxide equilibria are central to CO production in molten carbonate media. Determining whether molecular CO_2, carbonate, or a surface-derived species dominates the initial electron-transfer step remains an important mechanistic question. Although the

exact elementary pathway remains unresolved, both mechanistic frameworks highlight the central role of oxide-ion chemistry and the electrode interface in molten salt CO_2 electroreduction. The overall molten-carbonate electrolysis scheme and cathodic reaction pathways are summarized in Figure 8a.

Table 5. Proposed mechanism for the electrochemical reduction of CO_2 to CO in molten carbonate media, considering molecular CO_2 as the electroactive species. All elementary reaction steps occur at the cathode unless otherwise indicated. The anodic and overall cell reactions are included for completeness.

Step	Label
$CO_2 + * \rightarrow *CO_2$	Adsorption
$*CO_2 + e^- \rightarrow *CO_2^{\bullet -}$	Electron transfer
$*CO_2^{\bullet -} + e^- \rightarrow *CO_2^{2-}$	Second electron transfer
$*CO_2^{2-} \rightarrow *CO + O^{2-}$	De-oxygenation
$*CO \rightarrow CO + *$	Desorption
(Cathode) $CO_2 + 2\,e^- \rightarrow CO + O^{2-}$	Cathodic half-reaction
(Anode) $O^{2-} \rightarrow \frac{1}{2}\,O_2 + 2\,e^-$	Anodic half-reaction
(Cell) $CO_2 \rightarrow CO + \frac{1}{2}\,O_2$	Overall cell reaction

(*) denotes an active site or an intermediate adsorbed on the catalyst surface.

Table 6. Proposed mechanism for the electrochemical reduction of CO_2 to CO in molten carbonate media, considering carbonate ions (CO_3^{2-}) as the electroactive species. All elementary reaction steps occur at the cathode unless otherwise indicated. The anodic and overall cell reactions are included for completeness.

Step	Label
$CO_3^{2-} + * \rightarrow *CO_3^{2-}$	Adsorption
$*CO_3^{2-} + e^- \rightarrow *CO_2^{\bullet -} + O^{2-}$	First electron transfer coupled with de-oxygenation
$*CO_2^{\bullet -} + e^- \rightarrow *CO + O^{2-}$	Second electron transfer coupled with de-oxygenation
$*CO \rightarrow CO + *$	Desorption
(Cathode) $CO_3^{2-} + 2\,e^- \rightarrow CO + 2\,O^{2-}$	Cathodic half-reaction
(Anode) $O^{2-} \rightarrow \frac{1}{2}\,O_2 + 2\,e^-$	Anodic half-reaction
(Cell) $CO_3^{2-} \rightarrow CO + O^{2-} + \frac{1}{2}\,O_2$	Overall cell reaction

(*) denotes an active site or an intermediate adsorbed on the catalyst surface.

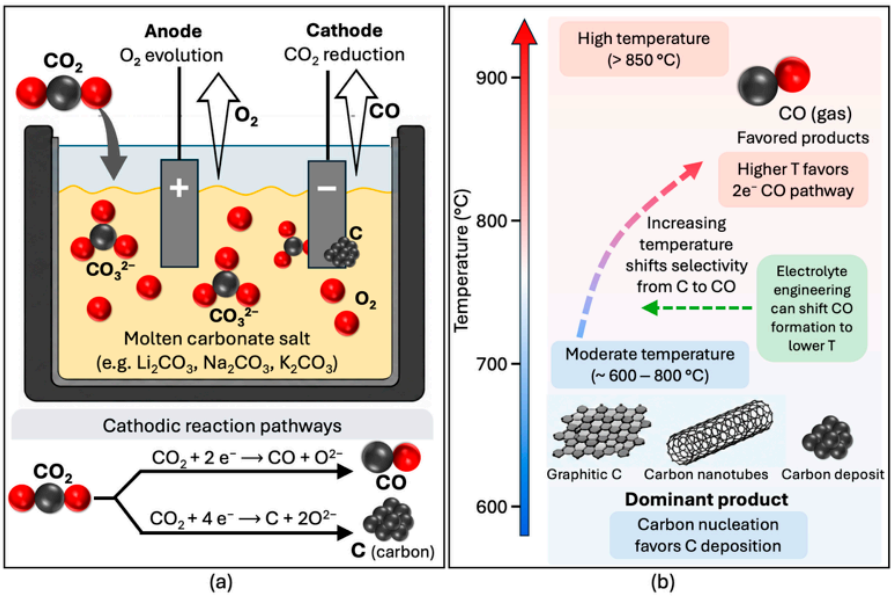


Figure 8. Molten salt CO_2 electroreduction. (**a**) Schematic of a molten-carbonate electrolysis cell and the main cathodic pathways leading to CO or carbon. (**b**) Qualitative effect of temperature on product selectivity, showing the shift from carbon formation at moderate temperature to CO formation at higher temperature.

5.2. Temperature, Thermodynamics, and CO/Carbon Selectivity

The absence of proton-coupled reaction pathways fundamentally alters the accessible product distribution in molten salts. Whereas aqueous CO_2 electroreduction can yield hydrocarbons and oxygenates through successive proton–electron transfer steps, molten carbonate electrolysis is dominated by CO and solid-carbon formation. Under these high-temperature, anhydrous conditions, reduction proceeds through electron transfer to CO_2-derived or carbonate-derived species, with product selectivity governed by the thermodynamics and kinetics of the molten salt environment.

As temperature increases, the energetic requirement for CO_2 splitting decreases and the two-electron pathway to CO becomes increasingly favorable, whereas carbon formation can remain kinetically competitive once carbon nucleates on the cathode surface and promotes continued deposition. This temperature-dependent shift in product selectivity is summarized in Figure 8b and distinguishes molten salts from aqueous and room-temperature ionic-liquid systems.

In molten carbonate electrolysis, solid carbon is frequently the predominant product at moderate temperatures (~600–800 °C) [102,103]. Although the identity of the electroactive species remains debated, many mechanistic studies propose that carbon forms through the electroreduction of carbonate species at the cathode surface. Above ~850 °C, particularly around 900 °C, carbon monoxide becomes the favored product [104], consistent with both thermodynamic predictions [105] and experimental reports using Li_2CO_3 or Li_2CO_3–K_2CO_3 melts with titanium [101] or gold [106] cathodes, where near-unity Faradaic efficiency toward CO has been observed [107].

Thermodynamic analyses have further quantified this temperature dependence. Ren et al. calculated the full-cell potentials for CO_2 reduction to CO and solid carbon as a function of temperature, identifying a crossover near 900 °C at which CO evolution becomes energetically more favorable than carbon deposition [108]. They also showed that increasing CO_2 pressure decreases the required cell potential, particularly for CO formation [109].

Although temperatures near 900 °C are commonly associated with favorable CO formation in molten-carbonate electrolysis, electrolyte engineering can shift this selectivity to substantially lower temperatures. Hu et al. showed that borate addition to a LiCl–Li_2CO_3 melt enabled CO evolution at ~550 °C with ~90% Faradaic efficiency [110,111]. Similarly, Ji et al. reported CO-rich syngas containing 33.6% CO at 550 °C in a carbonate/hydroxide melt [112]. These studies demonstrate that melt composition can modify the thermodynamic and kinetic conditions governing CO formation, allowing high-temperature selectivity trends to be shifted through electrolyte design.

In addition to temperature, the interaction between the cathode material and carbon-derived intermediates can influence product formation. Yu et al. showed that substrate-dependent carbon-binding strength helps determine whether molten-carbonate electrolysis yields graphitic carbon, metal carbides, or more weakly bound carbonaceous products [113]. Metals with intermediate carbon affinity, such as Fe, Ni, Co, and Cr, favor graphitic growth, whereas stronger carbon-binding metals promote carbide formation and weaker-binding metals such as Cu favor less ordered carbon. These results indicate that, as in aqueous CO_2 reduction, adsorption energetics provide an additional descriptor of selectivity beyond electrolyte thermodynamics alone.

Outside carbonate-based systems, CO formation has also been demonstrated in $CaCl_2$–CaO melts, although carbon formation remained competitive and the reported current efficiency toward CO was 36.9% under the reported condition [114].

5.3. Potential Roles of Metallic Nanoparticles

Although electrolyte composition and temperature strongly influence CO/carbon selectivity, modifying the cathode surface through catalyst design may provide an additional means of controlling product formation. Metallic nanoparticles could potentially alter intermediate stabilization, carbon nucleation, and interfacial reaction pathways, providing a complementary strategy to electrolyte engineering for promoting CO formation or suppressing carbon deposition.

Despite this potential, remarkably few studies have examined metallic nanoparticles specifically for molten salt CO_2-to-CO electroreduction. Existing nanoparticle-related studies have instead focused mainly on carbon formation or CO_2 capture, highlighting both the opportunities and the current lack of direct evidence for nanoparticle-controlled CO selectivity.

Pint and co-workers demonstrated electrochemical conversion of CO_2 into carbon nanotubes in molten carbonate electrolytes using Fe-based catalysts [115]. During electrolysis, thin metal-containing films evolved into nanoscale catalytic particles that controlled nanotube nucleation, growth, and diameter. Subsequent studies reinforced this picture. Liu et al. showed that Fe-, Ni-, and Cr-containing species can govern transition-metal-nucleated carbon nanotube growth [116], while Laasonen et al. demonstrated that dissolved and redeposited metals strongly influence the morphology of the carbon product [117]. More recently, Dipta et al. showed that controlled release of Fe and Ni species from pretreated alloy electrodes can generate catalytic nucleation sites and tune carbon nanotube growth [118]. Collectively, these studies indicate that metallic nanoparticles in molten-carbonate electrolysis have so far been exploited primarily to promote and control solid-carbon formation rather than to favor CO evolution.

Related molten-salt studies outside electrocatalysis also provide insight into how nanoparticles can modify carbon transport and chemical speciation within the electrolyte. Harada et al. dispersed MgO nanoparticles in molten nitrate-based salts as reactive CO_2 sorbents for continuous capture at 200–350 °C [119]. The MgO nanoparticles provided reactive oxide surfaces for carbonate formation, while the molten salt facilitated CO_2 transport and maintained the particles as a nonvolatile colloidal absorbent. This study illustrates how nanoparticle–molten salt interactions can influence CO_2 uptake and transport, properties that may also be relevant to the design of molten-salt electrochemical systems.

Together, these studies show that nanoparticles can influence carbon chemistry in molten salts through nucleation, surface reaction, and CO_2 capture, but direct demonstrations of metallic nanoparticles selectively promoting CO formation remain scarce. This gap contrasts sharply with aqueous and ionic-liquid systems and represents one of the clearest opportunities for future catalyst development in molten salt CO_2 electroreduction.

5.4. Electrode Compatibility, Corrosion, Durability, and Scale-Up

Electrode compatibility represents an additional challenge for molten-carbonate electrolysis because metallic components are exposed simultaneously to elevated temperature, strongly basic carbonate/oxide-ion environments, and electrochemical polarization. Corrosion is particularly important at the anode, where oxide ions are converted to O_2 and strongly oxidizing interfacial species can destabilize metallic surfaces and passive layers. The extent of degradation depends strongly on alloy composition, electrolyte composition and basicity, impurities, temperature, and operating conditions, making electrode-material selection an integral part of electrolyzer design rather than a secondary engineering consideration [120].

Several studies illustrate how strongly alloy composition influences durability. Frangini et al. evaluated five Inconel alloys as oxygen-evolving anodes in Li_2CO_3–Na_2CO_3–K_2CO_3 at 500 °C and found that Ti- and Al-containing Inconel 617, 718, and X-750 exhibited improved

passivation; Inconel 617 and X-750 showed particularly high stability under pulsed polarization, whereas continuous direct-current operation promoted rapid degradation [121]. Tang et al. demonstrated a complementary strategy using a Ni–Cu–Fe alloy, on which a protective multilayer consisting primarily of $NiFe_2O_4$, NiO, and a Cu-rich metallic layer formed during operation and enabled oxygen evolution for more than 600 h in molten Na_2CO_3–K_2CO_3 [122]. These results show that controlled formation of protective surface layers can be as important as the bulk alloy composition itself.

Compatibility is also important at the cathode and for other reactor components. Electrode composition can influence the availability of transition-metal species in molten-carbonate electrolysis [116], while studies comparing Ni, stainless steel, and Ni–Cr–Fe–Mo alloys in molten Li_2CO_3 at 750 °C directly detected Ni, Fe, and Cr in the electrolysis products, demonstrating that electrode dissolution or corrosion can introduce metallic species into the reaction environment [123]. More recent comparison of Ti, Ni, and Alloy X electrode combinations identified a Ti cathode–Ni anode pair as the most stable among the tested configurations [124]. Although these studies primarily examined carbon rather than selective CO production, the underlying materials constraints are directly relevant to CO_2-to-CO electrolysis because the electrodes and reactor hardware experience the same high-temperature molten-carbonate environment.

These durability issues become increasingly important during scale-up. Corrosion and metal dissolution can shorten electrode and reactor lifetimes, modify the electrochemical interface, contaminate the electrolyte or products, and complicate long-term operation. Consequently, practical scale-up requires simultaneous optimization of the cathode, oxygen-evolving anode, supports, current collectors, and containment materials. Corrosion-resistant Ni-based superalloys and passivating surface layers provide promising strategies, but long-duration materials testing under conditions optimized specifically for selective CO production remains limited.

5.5. Design Opportunities and Major Knowledge Gaps

Nanoparticle-based catalyst design for molten-salt CO_2-to-CO electroreduction remains largely unexplored, as most nanostructured studies have focused on carbon formation or material synthesis. Composition, particle size, surface structure, and support interactions may provide routes to favor CO formation and suppress carbon deposition, but systematic structure–activity relationships have not yet been established.

Major knowledge gaps also remain regarding the stability and identity of metallic nanoparticles under molten salt conditions. High temperatures can promote particle growth, restructuring, dissolution, or reaction with the electrolyte and electrode support, while the nature of the electroactive species and surface-bound intermediates remains incompletely resolved. Progress will therefore require direct characterization of catalyst evolution under operating conditions and systematic separation of nanoparticle effects from those arising from electrolyte composition, temperature, and electrode architecture.

6. Cross-Electrolyte Comparison and Future Perspectives

The three electrolyte classes impose fundamentally different reaction environments: aqueous systems are strongly influenced by proton availability, local pH, and competition with HER; ionic liquids introduce ion–surface interactions and organized interfacial structures; and molten salts are governed largely by carbonate–oxide chemistry, temperature, and competition with carbon formation. These differences are summarized in Figure 9.

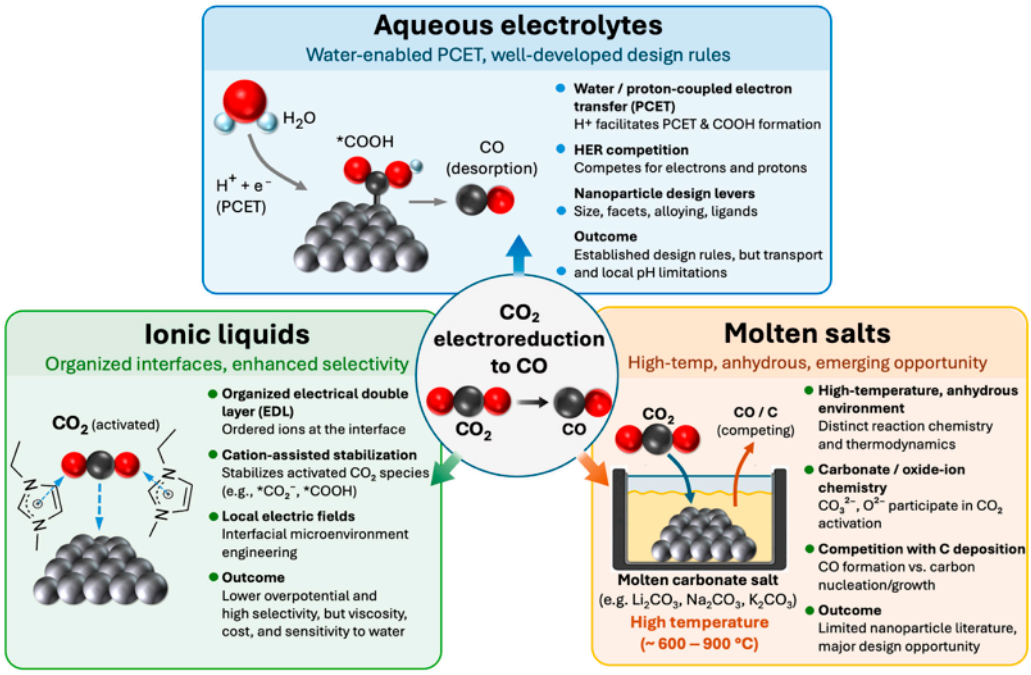


Figure 9. Electrolyte comparison. Aqueous electrolytes, ionic liquids, and molten salts provide distinct reaction environments that modify CO_2 activation, intermediate stabilization, competing reactions, and nanoparticle behavior. Across all three media, catalytic performance emerges from the coupled effects of electrolyte properties and catalyst structure. (*) denotes an intermediate adsorbed on the catalyst surface.

Nanoparticle descriptors therefore acquire different significance depending on the surrounding medium. In aqueous electrolytes, particle size, surface coordination, composition, oxidation state, ligands, and support interactions can alter the balance among *COOH formation, *CO desorption, and HER. In ionic liquids, these structural variables additionally influence ion adsorption, interfacial organization, and stabilization of CO_2-derived intermediates. Comparable nanoparticle-specific structure–activity relationships remain largely unresolved in molten salts, where high temperature, catalyst restructuring, carbon deposition, and interactions with the melt can dominate the electrode surface.

Despite these differences, selected high-performance examples provide a useful indication of the capabilities of each medium (Table 7). Faradaic efficiencies approaching or exceeding 95% and CO partial current densities above 100 mA cm^{-2} have been demonstrated in all three electrolyte classes. These values should not be interpreted as direct performance rankings, however, because Faradaic efficiency, current density, potential, durability, and energy requirements depend on electrolyte composition, water content, temperature, catalyst loading, electrode architecture, mass transport, cell configuration, and the reference scale used. The aqueous and ionic-liquid examples employ nanostructured metallic catalysts, whereas an equivalent nanoparticle-specific benchmark is not yet available for molten-salt CO production. The molten-salt example in Table 7 therefore represents the performance achievable in that reaction environment rather than the performance of a nanoparticle catalyst.

The comparison therefore reveals not only differences in operating conditions but also different levels of catalyst-design maturity. Aqueous systems currently provide the most developed nanoparticle structure–activity framework and can combine high CO selectivity with high current density. Ionic liquids provide additional opportunities for controlling interfacial chemistry through electrolyte composition and ion organization while maintaining high CO selectivity. Molten salts can also achieve high CO selectivity

and substantial current densities, but selective CO production remains governed primarily by temperature and electrolyte composition, with the role of metallic nanoparticles still poorly established.

Table 7. Illustrative high-performance examples of CO_2-to-CO electroreduction across aqueous, ionic-liquid, and molten-salt media. Electrode potentials and cell voltages are reported as given in the original studies and should not be compared directly because different reference scales and cell configurations were used.

Medium	Representative System	T (°C)	FE_{CO} (%)	j_{CO} * (mA cm^{-2})	Applied Potential	Cell Voltage	Durability † (h)
Aqueous	[33] CuNi-based nanostructured catalyst	~25	>95	> 399	~−1.0 V vs. RHE	—	24
Ionic liquid	[85] Ag(111)-dominant nanofoam/[BMIM][BF_4]	~25	99.4	≈125	−2.4 V vs. Ag/Ag^+	—	10
Molten salt	[101] Ti/Li_2CO_3	900	≥96, close to 100	≥127	—	1.0 ± 0.05 V **	120 continuous >700 cumulative

* j_{CO} values were taken from the original studies when reported; otherwise, they were calculated from the total current density and CO Faradaic efficiency as $j_{CO} = j \times FE_{CO}/100$. ** Li_2CO_3 decomposition potential: 0.866 ± 0.014 V; thermodynamic efficiency: 86 ± 5%; cathodic overpotential ≈80 mV at 132 mA cm^{-2}. † Durability corresponds to the long-term electrolysis test reported for each system and was not necessarily measured at the operating condition associated with the maximum j_{CO} listed in the table.

These differences emphasize the need for catalyst–electrolyte co-design, particularly in ionic-liquid and molten-salt systems where nanoparticle structure–activity relationships remain less established. Future studies should therefore combine catalyst characterization with systematic control of electrolyte composition, interfacial conditions, and mass transport. Data-driven approaches may further support this effort. Recent studies have demonstrated machine-learning-assisted screening of CO_2-reduction catalysts as well as data-driven design and screening of electrolyte properties, although broader application will require more standardized and comparable experimental datasets [125–127].

7. Conclusions

This review demonstrates that the performance of metallic nanoparticles for electrochemical CO_2 reduction to CO is determined by the coupled catalyst–electrolyte interface rather than by catalyst structure alone. Across aqueous, ionic-liquid, and molten-salt media, the reaction environment determines how nanoparticle composition, size, surface structure, oxidation state, and functionalization are expressed catalytically. Although high CO selectivity and substantial CO partial current densities have been achieved in all three electrolyte classes, differences in operating conditions, cell configuration, energy requirements, and durability prevent simple performance rankings.

Future progress will require more comparable performance benchmarks, long-duration evaluation of catalyst and electrolyte stability, and direct characterization of nanoparticle structure and interfacial chemistry under operating conditions. The largest knowledge gaps remain in ionic-liquid and molten-salt systems, where nanoparticle-specific structure–activity relationships are still much less developed than in aqueous media. Establishing these relationships will be essential for translating electrolyte-dependent control into more selective, stable, and practically viable CO_2-to-CO electrolysis systems.

Author Contributions: Conceptualization, L.G.-U.; methodology, L.G.-U.; literature investigation, L.G.-U., W.M. and D.P.; formal analysis, L.G.-U.; data curation, W.M. and D.P.; writing—original draft preparation, L.G.-U. and W.M.; writing—review and editing, L.G.-U., W.M. and D.P.; visualization,

L.G.-U. and W.M.; supervision, L.G.-U.; project administration, L.G.-U. All authors have read and agreed to the published version of the manuscript.

Funding: This work was supported by a PSC-CUNY Research Award from The City University of New York (Award # 67202-00 55, Cycle 55), the BMCC Foundation Fund (BFF), and the CUNY Research Scholars Program (CRSP).

Data Availability Statement: No new data were created or analyzed in this study. Data sharing is not applicable to this article.

Acknowledgments: During the preparation of this manuscript, the authors used OpenAI ChatGPT-5 and Google Gemini-3 to assist with language editing, rephrasing, and improving the clarity of author-prepared text. All scientific content, interpretations, references, and final revisions were reviewed and verified by the authors, who take full responsibility for the content of the publication. No AI-generated images were included in the paper.

Conflicts of Interest: The authors declare no conflicts of interest.

Abbreviations

The following abbreviations are used in this manuscript:

HER	Hydrogen evolution reaction
FE_{CO}	Faradaic efficiency toward CO
j	Current density
j_{CO}	Partial current density toward CO
ECSA	Electrochemically active surface area
TOF	Turnover frequency
PCET	Proton-coupled electron transfer
RHE	Reversible hydrogen electrode
NC	N-doped carbon
IL	Ionic liquid
EMIM	1-ethyl-3-methylimidazolium
BMIM	1-butyl-3-methylimidazolium
DFT	Density functional theory

References

1. Berthelot, M. Recherches sur les métalloïdes et leurs composés. *Ann. Chim. Phys.* **1869**, *16*, 408–429.
2. Royer, M. Réduction de l'acide carbonique en acide formique. *Compt. Rend.* **1870**, *70*, 731–732.
3. Hori, Y.; Kikuchi, K.; Suzuki, S. Production of CO and CH_4 in electrochemical reduction of CO_2 at metal electrodes in aqueous hydrogencarbonate solution. *Chem. Lett.* **1985**, *14*, 1695–1698. [CrossRef]
4. Garza, A.J.; Bell, A.T.; Head-Gordon, M. Mechanism of CO_2 reduction at copper surfaces: Pathways to C_2 products. *J. Phys. Chem. Lett.* **2018**, *9*, 236–242.
5. Marchetti, C. On geoengineering and the CO_2 problem. *Clim. Change* **1977**, *1*, 59–68. [CrossRef]
6. Costentin, C.; Robert, M.; Savéant, J.-M. Catalysis of the electrochemical reduction of carbon dioxide. *Chem. Soc. Rev.* **2013**, *42*, 2423–2436. [CrossRef] [PubMed]
7. Bierhals, J. Carbon Monoxide. In *Ullmann's Encyclopedia of Industrial Chemistry*, 6th ed.; Elvers, B., Hawkins, S., Russey, W.E., Eds.; Wiley-VCH: Weinheim, Germany, 2003; Volume 6, pp. 457–472
8. Bertleff, W. Carbonylation. In *Ullmann's Encyclopedia of Industrial Chemistry*, 6th ed.; Elvers, B., Hawkins, S., Russey, W.E., Eds.; Wiley-VCH: Weinheim, Germany, 2003; Volume 6, pp. 473–492.
9. Anderson, R.B. *The Fischer–Tropsch Synthesis*; Academic Press: New York, NY, USA, 1984.
10. U.S. Department of Energy; Office of Fossil Energy and Carbon Management. *Carbon Conversion Market Background & Opportunities*; U.S. Department of Energy: Washington, DC, USA, 2024; p. 4. Available online: https://www.energy.gov/hgeo/events/carbon-conversion-market-background-opportunities (accessed on 12 October 2025).
11. Grand View Research, Inc. *Carbon Monoxide Market Size to Reach USD 6.97 Billion by 2030*; Grand View Research: San Francisco, CA, USA, 2025. Available online: www.grandviewresearch.com/press-release/global-carbon-monoxide-market (accessed on 12 October 2025).
12. Álvarez, A.; Borges, M.; Corral-Pérez, J.J.; Giner Olcina, J.; Hu, L.; Cornu, D.; Huang, R.; Stoian, D.; Urakawa, A. CO_2 activation over catalytic surfaces. *ChemPhysChem* **2017**, *18*, 3135–3141. [CrossRef] [PubMed]

13. Jin, S.; Hao, Z.; Zhang, K.; Yan, Z.; Chen, J. Advances and challenges for the electrochemical reduction of CO_2 to CO: From fundamentals to industrialization. *Angew. Chem. Int. Ed.* **2021**, *60*, 20627–20648. [CrossRef] [PubMed]
14. Jouny, M.; Luc, W.; Jiao, F. High-rate electroreduction of carbon monoxide to multi-carbon products. *Nat. Catal.* **2018**, *1*, 748–755. Correction in *Nat. Catal.* **2018**, *1*, 1002. https://doi.org/10.1038/s41929-018-0196-0. [CrossRef]
15. Kondratenko, E.V.; Mul, G.; Baltrusaitis, J.; Larrazábal, G.O.; Pérez-Ramírez, J. Status and perspectives of CO_2 conversion into fuels and chemicals by catalytic, photocatalytic and electrocatalytic processes. *Energy Environ. Sci.* **2013**, *6*, 3112–3135. [CrossRef]
16. Chatenet, M.; Pollet, B.G.; Dekel, D.R.; Dionigi, F.; Deseure, J.; Millet, P.; Braatz, R.D.; Bazant, M.Z.; Eikerling, M.; Staffell, I.; et al. Water electrolysis: From textbook knowledge to the latest scientific strategies and industrial developments. *Chem. Soc. Rev.* **2022**, *51*, 4583–4762. [CrossRef] [PubMed]
17. Rosen, B.A.; Salehi-Khojin, A.; Thorson, M.R.; Zhu, W.; Whipple, D.T.; Kenis, P.J.A.; Masel, R.I. Ionic liquid-mediated selective conversion of CO_2 to CO at low overpotentials. *Science* **2011**, *334*, 643–644. [CrossRef]
18. DiMeglio, J.L.; Rosenthal, J. Selective conversion of CO_2 to CO with high efficiency using an inexpensive bismuth-based electrocatalyst. *J. Am. Chem. Soc.* **2013**, *135*, 8798–8801. [CrossRef] [PubMed]
19. Hollingsworth, N.; Taylor, S.R.; Galante, M.T.; Jacquemin, J.; Longo, C.; Holt, K.B.; de Leeuw, N.H.; Hardacre, C. Reduction of carbon dioxide to formate at low overpotential using a superbase ionic liquid. *Angew. Chem. Int. Ed.* **2015**, *54*, 14164–14168. [CrossRef]
20. Yin, H.; Mao, X.; Tang, D.; Xiao, W.; Xing, L.; Zhu, H.; Wang, D.; Sadoway, D.R. Capture and electrochemical conversion of CO_2 to value-added carbon and oxygen by molten salt electrolysis. *Energy Environ. Sci.* **2013**, *6*, 1538–1545. [CrossRef]
21. Jiang, R.; Gao, M.; Mao, X.; Wang, D. Advancements and potentials of molten salt CO_2 capture and electrochemical transformation (MSCC-ET) process. *Curr. Opin. Electrochem.* **2019**, *17*, 38–46. [CrossRef]
22. Weng, W.; Tang, L.; Xiao, W. Capture and electro-splitting of CO_2 in molten salts. *J. Energy Chem.* **2019**, *28*, 128–143. [CrossRef]
23. Thorson, M.R.; Siil, K.I.; Kenis, P.J.A. Effect of cations on the electrochemical conversion of CO_2 to CO. *J. Electrochem. Soc.* **2013**, *160*, F69–F74. [CrossRef]
24. Murata, A.; Hori, Y. Product selectivity affected by cationic species in electrochemical reduction of CO_2 and CO at a Cu electrode. *Bull. Chem. Soc. Jpn.* **1991**, *64*, 123–127. [CrossRef]
25. Nguyen, D.L.T.; Jee, M.S.; Oh, H.S.; Min, B.K.; Hwang, Y.J. Effect of halides on nanoporous Zn-based catalysts for highly efficient electroreduction of CO_2 to CO. *Catal. Commun.* **2018**, *114*, 109–113. [CrossRef]
26. Fan, Q.; Zhang, M.; Jia, M.; Liu, S.; Qiu, J.; Sun, Z. Electrochemical CO_2 reduction to C_2+ species: Heterogeneous electrocatalysts, reaction pathways, and optimization strategies. *Mater. Today Energy* **2018**, *10*, 280–301. [CrossRef]
27. Kortlever, R.; Shen, J.; Schouten, K.J.P.; Calle-Vallejo, F.; Koper, M.T.M. Catalysts and reaction pathways for the electrochemical reduction of carbon dioxide. *J. Phys. Chem. Lett.* **2015**, *6*, 4073–4082. [CrossRef] [PubMed]
28. Cave, E.R.; Shi, C.; Kuhl, K.P.; Hatsukade, T.; Abram, D.N.; Hahn, C.; Chan, K.; Jaramillo, T.F. Trends in the catalytic activity of hydrogen evolution during CO_2 electroreduction on transition metals. *ACS Catal.* **2018**, *8*, 3035–3040. [CrossRef]
29. Zhang, M.; Wang, K.; Huang, K.; Tao, H.; Su, X.; Liu, W.; Fu, S.; Guo, H.; Lian, C.; Wu, M.; et al. Semi-ionic C–F bonds modulate hydrogen dynamics for selective CO_2-to-CH_4electroreduction on carbon quantum dots. *Angew. Chem. Int. Ed.* **2026**, *65*, e3749916. [CrossRef] [PubMed]
30. Zhao, S.; Jin, R.; Jin, R. Opportunities and challenges in CO_2 reduction by gold- and silver-based electrocatalysts: From bulk metals to nanoparticles and atomically precise nanoclusters. *ACS Energy Lett.* **2018**, *3*, 452–462. [CrossRef]
31. Peterson, A.A.; Nørskov, J.K. Activity descriptors for CO_2 electroreduction to methane on transition-metal catalysts. *J. Phys. Chem. Lett.* **2012**, *3*, 251–258. [CrossRef]
32. Jia, G.; Wang, Y.; Sun, M.; Zhang, H.; Li, L.; Shi, Y.; Zhang, L.; Cui, X.; Lo, T.W.B.; Huang, B.; et al. Size effects of highly dispersed bismuth nanoparticles on electrocatalytic reduction of carbon dioxide to formic acid. *J. Am. Chem. Soc.* **2023**, *145*, 14133–14142. [CrossRef] [PubMed]
33. Pan, W.; Wang, P.; Fan, L.; Chen, K.; Yi, L.; Huang, J.; Cai, P.; Liu, X.; Chen, Q.; Wang, G.; et al. Cu–Ni alloy decorating N-doped carbon nanosheets toward high-performance electrocatalysis of mildly acidic CO_2 reduction. *Inorg. Chem. Front.* **2023**, *10*, 2276–2284. [CrossRef]
34. Yang, T.; Xie, W.; Tian, N.; Liu, X.-H.; Zhang, X. CuNi alloy nanoparticles embedded in N-doped carbon framework for electrocatalytic reduction of CO_2 to CO. *J. Alloys Compd.* **2022**, *904*, 164042. [CrossRef]
35. Kim, D.; Xie, C.; Becknell, N.; Yu, Y.; Karamad, M.; Chan, K.; Crumlin, E.J.; Nørskov, J.K.; Yang, P. Electrochemical activation of CO_2 through atomic ordering transformations of AuCu nanoparticles. *J. Am. Chem. Soc.* **2017**, *139*, 8329–8336. [CrossRef] [PubMed]
36. Ismail, A.M.; Samu, G.F.; Balog, Á.; Csapó, E.; Janáky, C. Composition-dependent electrocatalytic behavior of Au–Sn bimetallic nanoparticles in carbon dioxide reduction. *ACS Energy Lett.* **2019**, *4*, 48–53. [CrossRef]

37. Zhu, W.; Michalsky, R.; Metin, Ö.; Lv, H.; Guo, S.; Wright, C.J.; Sun, X.; Peterson, A.A.; Sun, S. Monodisperse Au nanoparticles for selective electrocatalytic reduction of CO_2 to CO. *J. Am. Chem. Soc.* **2013**, *135*, 16833–16836. Correction in *J. Am. Chem. Soc.* **2017**, *139*, 9408. https://doi.org/10.1021/jacs.7b05685. [CrossRef] [PubMed]
38. Mistry, H.; Reske, R.; Zeng, Z.; Zhao, Z.J.; Greeley, J.; Strasser, P.; Roldan Cuenya, B. Exceptional size-dependent activity enhancement in the electroreduction of CO_2 over Au nanoparticles. *J. Am. Chem. Soc.* **2014**, *136*, 16473–16476. [CrossRef] [PubMed]
39. Sedano Varo, E.; Tankard, R.E.; Kryger-Baggesen, J.; Jinschek, J.; Helveg, S.; Chorkendorff, I.; Damsgaard, C.D.; Kibsgaard, J. Gold nanoparticles for CO_2 electroreduction: An optimum defined by size and shape. *J. Am. Chem. Soc.* **2024**, *146*, 2015–2023. [CrossRef] [PubMed]
40. Gao, D.; Zhou, H.; Wang, J.; Miao, S.; Yang, F.; Wang, G.; Wang, J.; Bao, X. Size-dependent electrocatalytic reduction of CO_2 over Pd nanoparticles. *J. Am. Chem. Soc.* **2015**, *137*, 4288–4291. [CrossRef]
41. Liu, S.; Tao, H.; Zeng, L.; Liu, Q.; Xu, Z.; Liu, Q.; Luo, J.-L. Shape-dependent electrocatalytic reduction of CO_2 to CO on triangular silver nanoplates. *J. Am. Chem. Soc.* **2017**, *139*, 2160–2163. [CrossRef] [PubMed]
42. Reske, R.; Mistry, H.; Behafarid, F.; Roldan Cuenya, B.; Strasser, P. Particle size effects in the catalytic electroreduction of CO_2 on Cu nanoparticles. *J. Am. Chem. Soc.* **2014**, *136*, 6978–6986. [CrossRef] [PubMed]
43. Xu, K.; Zheng, S.; Li, Y.; Chu, H.; Xiong, Q.; Mei, Z.; Zhao, Q.; Yang, L.; Li, S.; Pan, F. Constructing low-valent Ni nanoparticles for highly selective CO_2 reduction. *Chin. Chem. Lett.* **2022**, *33*, 424–427. [CrossRef]
44. Kim, C.; Jeon, H.S.; Eom, T.; Jee, M.S.; Kim, H.; Friend, C.M.; Min, B.K.; Hwang, Y.J. Achieving selective and efficient electrocatalytic activity for CO_2 reduction using immobilized silver nanoparticles. *J. Am. Chem. Soc.* **2015**, *137*, 13844–13850. [CrossRef] [PubMed]
45. Zhang, C.; Zhang, W.; Karadas, F.; Low, J.; Long, R.; Liang, C.; Wang, J.; Li, Z.; Xiong, Y. Laser-ablation-assisted strain engineering of gold nanoparticles for selective electrochemical CO_2 reduction. *Nanoscale* **2022**, *14*, 7702–7710. [CrossRef] [PubMed]
46. Ghosh, M.; Saha, P.; Roy, S.; Barman, S.; Pillai, P.; Dey, A.; Khan, S. Cyclic(alkyl)(amino)carbene-stabilized gold nanoparticles for selective CO_2 reduction. *ACS Catal.* **2024**, *14*, 7011–7019. [CrossRef]
47. Souza, M.L.; Lima, F.H. Dibenzyldithiocarbamate-functionalized small gold nanoparticles as selective catalysts for the electrochemical reduction of CO_2 to CO. *ACS Catal.* **2021**, *11*, 12208–12219. [CrossRef]
48. Jia, M.; Choi, C.; Wu, T.-S.; Ma, C.; Kang, P.; Tao, H.; Fan, Q.; Hong, S.; Liu, S.; Soo, Y.-L.; et al. Carbon-supported Ni nanoparticles for efficient CO_2 electroreduction. *Chem. Sci.* **2018**, *9*, 8775–8780. [CrossRef] [PubMed]
49. Li, M.; Wang, J.; Cong, X.; Sun, Y.; Liu, Q.; Miao, Z.; Li, Z.; Wang, L. Confined Ni nanoparticles in N-doped carbon nanotubes for excellent pH-universal industrial-level electrocatalytic CO_2 reduction and Zn–CO_2 battery. *J. Colloid Interface Sci.* **2024**, *657*, 738–747. [CrossRef] [PubMed]
50. Cheng, Q.; Mao, K.; Ma, L.; Yang, L.; Zou, L.; Zou, Z.; Hu, Z.; Yang, H. Encapsulation of iron nitride by Fe–N–C shell enabling highly efficient electroreduction of CO_2 to CO. *ACS Energy Lett.* **2018**, *3*, 1205–1211. [CrossRef]
51. Ren, W.; Tan, X.; Jia, C.; Krammer, A.; Sun, Q.; Qu, J.; Smith, S.C.; Schueler, A.; Hu, X.; Zhao, C. Electronic regulation of nickel single atoms by confined nickel nanoparticles for energy-efficient CO_2 electroreduction. *Angew. Chem. Int. Ed.* **2022**, *61*, e202203335. [CrossRef] [PubMed]
52. Seong, H.; Efremov, V.; Park, G.; Kim, H.; Yoo, J.S.; Lee, D. Atomically precise gold nanoclusters as model catalysts for identifying active sites for electroreduction of CO_2. *Angew. Chem. Int. Ed.* **2021**, *60*, 14563–14570. [CrossRef] [PubMed]
53. Yuan, S.F.; He, R.L.; Han, X.S.; Wang, J.Q.; Guan, Z.J.; Wang, Q.M. Robust gold nanocluster protected with amidinates for electrocatalytic CO_2 reduction. *Angew. Chem. Int. Ed.* **2021**, *60*, 14345–14349. [CrossRef] [PubMed]
54. Wang, Y.-M.; Yan, F.-Q.; Wang, Q.-Y.; Du, C.-X.; Wang, L.-Y.; Li, B.; Wang, S.; Zang, S.-Q. Single-atom tailored atomically precise nanoclusters for enhanced electrochemical reduction of CO_2-to-CO activity. *Nat. Commun.* **2024**, *15*, 1843. [CrossRef] [PubMed]
55. Gao, Z.-H.; Wei, K.; Wu, T.; Dong, J.; Jiang, D.-E.; Sun, S.; Wang, L.-S. A heteroleptic gold hydride nanocluster for efficient and selective electrocatalytic reduction of CO_2 to CO. *J. Am. Chem. Soc.* **2022**, *144*, 5258–5262. [CrossRef] [PubMed]
56. Ma, X.; Sun, F.; Qin, L.; Liu, Y.; Kang, X.; Wang, L.; Jiang, D.-E.; Tang, Q.; Tang, Z. Electrochemical CO_2 reduction catalyzed by atomically precise alkynyl-protected Au_7Ag_8, Ag_9Cu_6, and $Au_2Ag_8Cu_5$ nanoclusters: Probing the effect of multi-metal core on selectivity. *Chem. Sci.* **2022**, *13*, 10149–10158. [PubMed]
57. Yamada, T.; Iwase, K.; Todoroki, N.; Honma, I. High specific activity during electrochemical CO_2 reduction through homogeneous deposition of gold nanoparticles on gas diffusion electrodes. *ACS Appl. Energy Mater.* **2025**, *8*, 821–829. [CrossRef]
58. Burdyny, T.; Smith, W.A. CO_2 reduction on gas-diffusion electrodes and why catalytic performance must be assessed at commercially relevant conditions. *Energy Environ. Sci.* **2019**, *12*, 1442–1453. [CrossRef]
59. Li, Y.C.; Lee, G.; Yuan, T.; Wang, Y.; Nam, D.H.; Wang, Z.; García de Arquer, F.P.; Lum, Y.; Dinh, C.-T.; Voznyy, O.; et al. CO_2 electroreduction from carbonate electrolyte. *ACS Energy Lett.* **2019**, *4*, 1427–1431. [CrossRef]
60. Yun, H.; Kim, J.; Choi, W.; Han, M.H.; Park, J.H.; Oh, H.S.; Won, D.H.; Kwak, K.; Hwang, Y.J. Understanding morphological degradation of Ag nanoparticle during electrochemical CO_2 reduction reaction by identical-location observation. *Electrochim. Acta* **2021**, *371*, 137795. [CrossRef]

61. Wang, Y.; Xue, R.; Wang, N.; Ma, L.; Chen, Y.; Yang, Q.; Yan, X.; Shadike, Z.; Shen, S.; Zhang, J. Stability and degradation mechanisms of silver–nickel nanoparticle catalysts for electrochemical CO_2 reduction. *Chem. Commun.* **2026**, *62*, 9455–9458. [CrossRef] [PubMed]
62. Yan, K.; Lee, S.-W.; Yap, K.M.K.; Mule, A.S.; Hannagan, R.T.; Matthews, J.E.; Kamat, G.A.; Lee, D.U.; Stevens, M.B.; Nielander, A.C.; et al. On-line inductively coupled plasma mass spectrometry reveals material degradation dynamics of Au and Cu catalysts during electrochemical CO_2 reduction. *J. Am. Chem. Soc.* **2025**, *147*, 4079–4088. [CrossRef] [PubMed]
63. Mistry, H.; Choi, Y.-W.; Bagger, A.; Scholten, F.; Bonifacio, C.S.; Sinev, I.; Divins, N.J.; Zegkinoglou, I.; Jeon, H.S.; Kisslinger, K.; et al. Enhanced carbon dioxide electroreduction to carbon monoxide over defect-rich plasma-activated silver catalysts. *Angew. Chem. Int. Ed.* **2017**, *56*, 11394–11398. [CrossRef] [PubMed]
64. Hasa, B.; Zhao, Y.; Jiao, F. In situ/operando characterization techniques of electrochemical CO_2 reduction. *Annu. Rev. Chem. Biomol. Eng.* **2023**, *14*, 165–185. [CrossRef] [PubMed]
65. Burwell, T.; Thangamuthu, M.; Fernandes, J.A.; Khlobystov, A.N. Mapping reaction pathways and catalyst dynamics in electrochemical CO_2 reduction through in situ and operando characterisation. *Chem. Commun.* **2026**, *62*, 11802–11821. [CrossRef] [PubMed]
66. Firet, N.J.; Smith, W.A. Probing the reaction mechanism of CO_2 electroreduction over Ag films via operando infrared spectroscopy. *ACS Catal.* **2017**, *7*, 606–612. [CrossRef]
67. Guzmán, H.; Zammillo, F.; Roldán, D.; Galletti, C.; Russo, N.; Hernández, S. Investigation of gas diffusion electrode systems for the electrochemical CO_2 conversion. *Catalysts* **2021**, *11*, 482. [CrossRef]
68. Yang, H.; Lin, Q.; Zhang, C.; Yu, X.; Cheng, Z.; Li, G.; Hu, Q.; Ren, X.; Zhang, Q.; Liu, J.; et al. Carbon dioxide electroreduction on single-atom nickel decorated carbon membranes with industry-compatible current densities. *Nat. Commun.* **2020**, *11*, 593. [CrossRef] [PubMed]
69. Mohammed, S.A.S.; Yahya, W.Z.N.; Bustam, M.A.; Kibria, M.G. Elucidation of the roles of ionic liquid in CO_2 electrochemical reduction to value-added chemicals and fuels. *Molecules* **2021**, *26*, 6962. [CrossRef] [PubMed]
70. Tan, X.; Sun, X.; Han, B. Ionic liquid-based electrolytes for CO_2 electroreduction and CO_2 electroorganic transformation. *Natl. Sci. Rev.* **2022**, *9*, nwab022. [CrossRef] [PubMed]
71. Li, Y.; Li, F.; Laaksonen, A.; Wang, C.; Cobden, P.; Boden, P.; Liu, Y.; Zhang, X.; Ji, X. Electrochemical CO_2 reduction with ionic liquids: Review and evaluation. *Ind. Chem. Mater.* **2023**, *1*, 410–430. [CrossRef]
72. Cui, Y.; He, B.; Liu, X.; Sun, J. Ionic liquids-promoted electrocatalytic reduction of carbon dioxide. *Ind. Eng. Chem. Res.* **2020**, *59*, 20235–20252. [CrossRef]
73. Faggion, D., Jr.; Gonçalves, W.D.; Dupont, J. CO_2 electroreduction in ionic liquids. *Front. Chem.* **2019**, *7*, 102. [CrossRef] [PubMed]
74. Lim, H.-K.; Kwon, Y.; Kim, H.S.; Jeon, J.; Kim, Y.-H.; Lim, J.-A.; Kim, B.-S.; Choi, J.; Kim, H. Insight into the microenvironments of the metal–ionic liquid interface during electrochemical CO_2 reduction. *ACS Catal.* **2018**, *8*, 2420–2427. [CrossRef]
75. Wang, Y.; Hatakeyama, M.; Ogata, K.; Wakabayashi, M.; Jin, F.; Nakamura, S. Activation of CO_2 by ionic liquid EMIM–BF_4 in the electrochemical system: A theoretical study. *Phys. Chem. Chem. Phys.* **2015**, *17*, 23521–23531. [CrossRef] [PubMed]
76. Lau, G.P.; Schreier, M.; Vasilyev, D.; Scopelliti, R.; Grätzel, M.; Dyson, P.J. New insights into the role of imidazolium-based promoters for the electroreduction of CO_2 on a silver electrode. *J. Am. Chem. Soc.* **2016**, *138*, 7820–7823. [CrossRef] [PubMed]
77. Feng, J.; Zeng, S.; Feng, J.; Dong, H.; Zhang, X. CO_2 electroreduction in ionic liquids: A review. *Chin. J. Chem.* **2018**, *36*, 961–970. [CrossRef]
78. Coskun, O.K.; Bagbudar, Z.; Khokhar, V.; Dongare, S.; Warburton, R.E.; Gurkan, B. Synergistic effects of the electric field induced by imidazolium rotation and hydrogen bonding in electrocatalysis of CO_2. *J. Am. Chem. Soc.* **2024**, *146*, 23775–23785. [CrossRef] [PubMed]
79. Sun, L.; Ramesha, G.K.; Kamat, P.V.; Brennecke, J.F. Switching the reaction course of electrochemical CO_2 reduction with ionic liquids. *Langmuir* **2014**, *30*, 6302–6308. [CrossRef] [PubMed]
80. Liu, B.; Guo, W.; Gebbie, M.A. Tuning ionic screening to accelerate electrochemical CO_2 reduction in ionic liquid electrolytes. *ACS Catal.* **2022**, *12*, 9706–9716. [CrossRef]
81. Ju, F.; Zhang, J.; Lu, W. Efficient electrochemical reduction of CO_2 to CO in ionic liquid/propylene carbonate electrolyte on Ag electrode. *Catalysts* **2020**, *10*, 1102. [CrossRef]
82. Rosen, B.A.; Zhu, W.; Kaul, G.; Salehi-Khojin, A.; Masel, R.I. Water enhancement of CO_2 conversion on silver in 1-ethyl-3-methylimidazolium tetrafluoroborate. *J. Electrochem. Soc.* **2013**, *160*, H138–H141. [CrossRef]
83. Zhang, Z.; Chi, M.; Veith, G.M.; Zhang, P.; Lutterman, D.A.; Rosenthal, J.; Overbury, S.H.; Dai, S.; Zhu, H. Rational design of Bi nanoparticles for efficient electrochemical CO_2 reduction: The elucidation of size and surface condition effects. *ACS Catal.* **2016**, *6*, 6255–6264. [CrossRef]
84. Zhou, M.; Liu, H.; Yan, J.; Chen, Q.; Zhao, H.; Chen, R.; Liu, L. Theoretical insights into electrochemical CO_2 reduction by Bi-based catalysts: Single crystals versus mixed phases. *Chem. Eng. J.* **2025**, *514*, 163047. [CrossRef]

85. Zhang, H.; Zeng, S.; Jiang, C.; Peng, K.; Feng, J.; Yuan, L.; Li, X.; Xu, F.; Zhang, X. Efficient CO_2 electroreduction to CO facilitated by porous Ag(111)-dominant Ag nanofoams and cooperative ionic liquid electrolytes. *ChemCatChem* **2024**, *16*, e202400045. [CrossRef]
86. Lin, X.; Ma, W.; Sun, K.; Sun, B.; Fu, X.; Ren, X.; Liu, C.; Huang, J. $[AuAg_{26}(SR)_{18}S]^-$ Nanocluster: Open shell structure and high Faradaic efficiency in electrochemical reduction of CO_2 to CO. *J. Phys. Chem. Lett.* **2021**, *12*, 552–557. [CrossRef] [PubMed]
87. Salehi-Khojin, A.; Jhong, H.-R.M.; Rosen, B.A.; Zhu, W.; Ma, S.; Kenis, P.J.A.; Masel, R.I. Nanoparticle silver catalysts that show enhanced activity for carbon dioxide electrolysis. *J. Phys. Chem. C* **2013**, *117*, 1627–1632. [CrossRef]
88. Li, F.; Peng, K.; Jiang, C.; Zeng, S.; Zhang, X.; Ji, X. Boosting electrochemical reduction of CO_2 to CO using molecule-regulated Ag nanoparticle in ionic liquids. *Green Energy Environ.* **2025**, *10*, 813–820. [CrossRef]
89. Rudnev, A.V.; Kiran, K.; López, A.C.; Dutta, A.; Gjuroski, I.; Furrer, J.; Broekmann, P. Enhanced electrocatalytic CO formation from CO_2 on nanostructured silver foam electrodes in ionic liquid/water mixtures. *Electrochim. Acta* **2019**, *306*, 245–253. [CrossRef]
90. Vedharathinam, V.; Qi, Z.; Horwood, C.; Bourcier, B.; Stadermann, M.; Biener, J.; Biener, M. Using a 3D porous flow-through electrode geometry for high-rate electrochemical reduction of CO_2 to CO in ionic liquid. *ACS Catal.* **2019**, *9*, 10605–10611. [CrossRef]
91. Yang, D.; Zhu, Q.; Han, B. Electroreduction of CO_2 in ionic liquid-based electrolytes. *Innovation* **2020**, *1*, 100016. [CrossRef] [PubMed]
92. Costa, S.P.F.; Azevedo, A.M.O.; Pinto, P.C.A.G.; Saraiva, M.L.M.F.S. Environmental impact of ionic liquids: Recent advances in (eco)toxicology and (bio)degradability. *ChemSusChem* **2017**, *10*, 2321–2347. [CrossRef] [PubMed]
93. Bystrzanowska, M.; Pena-Pereira, F.; Marcinkowski, Ł.; Tobiszewski, M. How green are ionic liquids?—A multicriteria decision analysis approach. *Ecotoxicol. Environ. Saf.* **2019**, *174*, 455–458. [CrossRef] [PubMed]
94. Yuan, L.; Zhang, L.; Feng, J.; Jiang, C.; Feng, J.; Li, C.; Zeng, S.; Zhang, X. Upscaling studies for efficiently electric-driven CO_2 reduction to CO in ionic liquid-based electrolytes. *Chem. Eng. J.* **2022**, *450*, 138378. [CrossRef]
95. Fortunati, A.; Risplendi, F.; Re Fiorentin, M.; Cicero, G.; Parisi, E.; Castellino, M.; Simone, E.; Iliev, B.; Schubert, T.J.S.; Russo, N.; et al. Understanding the role of imidazolium-based ionic liquids in the electrochemical CO_2 reduction reaction. *Commun. Chem.* **2023**, *6*, 84. [CrossRef] [PubMed]
96. Dongare, S.; Coskun, O.K.; Cagli, E.; Lee, K.Y.C.; Rao, G.; Britt, R.D.; Berben, L.A.; Gurkan, B. A bifunctional ionic liquid for capture and electrochemical conversion of CO_2 to CO over silver. *ACS Catal.* **2023**, *13*, 7812–7821. [CrossRef] [PubMed]
97. Melo, C.I.; Rente, D.; Nunes da Ponte, M.; Bogel-Łukasik, E.; Branco, L.C. Carbon dioxide to methane using ruthenium nanoparticles: Effect of the ionic liquid media. *ACS Sustain. Chem. Eng.* **2019**, *7*, 11963–11969. [CrossRef]
98. Melo, C.I.; Szczepańska, A.; Bogel-Łukasik, E.; Nunes da Ponte, M.; Branco, L.C. Hydrogenation of carbon dioxide to methane by ruthenium nanoparticles in ionic liquid. *ChemSusChem* **2016**, *9*, 1081–1084. [CrossRef] [PubMed]
99. Sun, Q.; Zhao, Y.; Ren, W.; Zhao, C. Electroreduction of low concentration CO_2 at atomically dispersed Ni–N–C catalysts with nanoconfined ionic liquids. *Appl. Catal. B Environ.* **2022**, *304*, 120963. [CrossRef]
100. Kaplan, V.; Wachtel, E.; Lubomirsky, I. CO_2 to CO electrochemical conversion in molten $Li_2CO_3$is stable with respect to sulfur contamination. *J. Electrochem. Soc.* **2014**, *161*, F54–F57. [CrossRef]
101. Kaplan, V.; Wachtel, E.; Gartsman, K.; Feldman, Y.; Lubomirsky, I. Conversion of CO_2 to CO by electrolysis of molten lithium carbonate. *J. Electrochem. Soc.* **2010**, *157*, B552–B556. [CrossRef]
102. Gao, M.; Deng, B.; Chen, Z.; Tao, M.; Wang, D. Cathodic reaction kinetics for CO_2 capture and utilization in molten carbonates at mild temperatures. *Electrochem. Commun.* **2018**, *88*, 79–82. [CrossRef]
103. Ji, D.; Zhang, F.; Qiao, Z.; Zhang, J.; Wu, H.; Wang, G. Electrochemical synthesis and structural characteristics of new carbon-based materials generated in molten salts. *Appl. Sci.* **2022**, *12*, 9923. [CrossRef]
104. Zhu, F.; Ge, J.; Gao, Y.; Li, S.; Chen, Y.; Tu, J.; Wang, M.; Jiao, S. Molten salt electro-preparation of graphitic carbons. *Exploration* **2023**, *3*, 20210186. [CrossRef] [PubMed]
105. Chery, D.; Lair, V.; Cassir, M. CO_2 electrochemical reduction into CO or C in molten carbonates: A thermodynamic point of view. *Electrochim. Acta* **2015**, *160*, 74–81. [CrossRef]
106. Chery, D.; Albin, V.; Meléndez-Ceballos, A.; Lair, V.; Cassir, M. Mechanistic approach of the electrochemical reduction of CO_2 into CO at a gold electrode in molten carbonates by cyclic voltammetry. *Int. J. Hydrogen Energy* **2016**, *41*, 18706–18712. [CrossRef]
107. Zhu, Q.; Zeng, Y.; Zheng, Y. Overview of CO_2 capture and electrolysis technology in molten salts: Operational parameters and their effects. *Ind. Chem. Mater.* **2023**, *1*, 595–617. [CrossRef]
108. Ren, J.; Lau, J.; Lefler, M.; Licht, S. The minimum electrolytic energy needed to convert carbon dioxide to carbon by electrolysis in carbonate melts. *J. Phys. Chem. C* **2015**, *119*, 23342–23349. [CrossRef]
109. Li, F.F.; Lau, J.; Licht, S. Sungas instead of syngas: Efficient coproduction of CO and H_2 with a single beam of sunlight. *Adv. Sci.* **2015**, *2*, 1500260. [CrossRef] [PubMed]
110. Hu, L.; Deng, B.; Du, K.; Jiang, R.; Dou, Y.; Wang, D. Tunable selectivity and high efficiency of CO_2 electroreduction via borate-enhanced molten salt electrolysis. *iScience* **2020**, *23*, 101607. [CrossRef] [PubMed]

111. Hu, L.; Deng, B.; Yang, Z.; Wang, D. Buffering electrolyte alkalinity for highly selective and energy-efficient transformation of CO_2 to CO. *Electrochem. Commun.* **2020**, *121*, 106864. [CrossRef]
112. Ji, D.; Jia, Q.; Zhu, C.; Dong, W.; Wu, H.; Wang, G. A new, efficient conversion technology to transform ambient CO_2 to valuable, carbon-based fuel via molten salt electrochemistry. *Appl. Sci.* **2022**, *12*, 8874. [CrossRef]
113. Yu, R.; Du, K.; Deng, B.; Yin, H.; Wang, D. Unraveling the role of substrate materials in governing the carbon/carbide growth of molten carbonate electrolysis of CO_2. *Nanoscale* **2023**, *15*, 18707–18715. [CrossRef] [PubMed]
114. Matsuura, F.; Wakamatsu, T.; Natsui, S.; Kikuchi, T.; Suzuki, R.O. CO gas production by molten salt electrolysis from CO_2 gas. *ISIJ Int.* **2015**, *55*, 404–408. [CrossRef]
115. Douglas, A.; Carter, R.; Li, M.; Pint, C.L. Toward small-diameter carbon nanotubes synthesized from captured carbon dioxide: Critical role of catalyst coarsening. *ACS Appl. Mater. Interfaces* **2018**, *10*, 19010–19018. [CrossRef] [PubMed]
116. Liu, X.; Licht, G.; Wang, X.; Licht, S. Controlled transition metal nucleated growth of carbon nanotubes by molten electrolysis of CO_2. *Catalysts* **2022**, *12*, 137. [CrossRef]
117. Laasonen, E.; Sorvali, M.; Ruuskanen, V.; Niemelä, M.; Koiranen, T.; Ahola, J.; Mäkelä, J.M.; Joronen, T. The effect of metal dissolution on carbon production by high-temperature molten salt electrolysis. *J. CO_2 Util.* **2023**, *69*, 102390. [CrossRef]
118. Dipta, I.K.R.A.; Lee, C.W. Anode surface engineering for tunable carbon nanotube growth via integrated carbon capture and conversion in low-cost molten carbonates. *Int. J. Energy Res.* **2026**, *2026*, 4730702. [CrossRef]
119. Harada, T.; Brown, P.; Hatton, T.A. Nonvolatile colloidal dispersion of MgO nanoparticles in molten salts for continuous CO_2 capture at intermediate temperatures. *ACS Sustain. Chem. Eng.* **2019**, *7*, 7979–7986. [CrossRef]
120. Wang, P.; Du, K.; Yin, H.; Wang, D. Corrosion and protection of metallic materials in molten carbonates for concentrating solar power and molten carbonate electrolysis applications. *Corros. Commun.* **2023**, *11*, 58–71. [CrossRef]
121. Frangini, S.; Paoletti, C.; Della Seta, L. Corrosion of Inconel alloys for application as inert anodes in low-temperature molten carbonate electrolysis processes. *Int. J. Hydrogen Energy* **2021**, *46*, 14953–14961. [CrossRef]
122. Tang, D.; Zheng, K.; Yin, H.; Mao, X.; Sadoway, D.R.; Wang, D. Electrochemical growth of a corrosion-resistant multi-layer scale to enable an oxygen-evolution inert anode in molten carbonate. *Electrochim. Acta* **2018**, *279*, 250–257. [CrossRef]
123. Nur'aini, A.; Laasonen, E.; Ruuskanen, V.; Niemelä, M.; Koiranen, T.; Kauranen, P.; Ahola, J. An investigation of non-noble metal electrodes for carbon dioxide electrolysis in molten lithium carbonate. *Int. J. Electrochem. Sci.* **2024**, *19*, 100499. [CrossRef]
124. Nur'aini, A.; Laasonen, E.; Ruuskanen, V.; Koiranen, T.; Kauranen, P.; Ahola, J. Investigation of electrode material and applied current density in molten carbonate electrolysis. *J. Ind. Eng. Chem.* **2025**, *144*, 792–805. [CrossRef]
125. Zou, S.; Luo, L.; Wang, G.; Shen, H.; Bai, H.; Wen, G.; Ren, B.; Wang, S. Machine learning-driven high-throughput screening of electrocatalysts and electrolytes for electrochemical surfaces and interfaces. *Chem. Commun.* **2026**, *62*, 11295–11317. [CrossRef] [PubMed]
126. Raj, K.; Bliss, M.; Nandigama, M.P.; Rajput, N.N. Data-driven molecular design rules for electrolytes in CO_2 electroreduction. *Cell Rep. Phys. Sci.* **2026**, *7*, 103390. [CrossRef]
127. Zhong, M.; Tran, K.; Min, Y.; Wang, C.; Wang, Z.; Dinh, C.-T.; De Luna, P.; Yu, Z.; Sedighian Rasouli, A.; Brodersen, P.; et al. Accelerated discovery of CO_2 electrocatalysts using active machine learning. *Nature* **2020**, *581*, 178–183. [CrossRef] [PubMed]

Disclaimer/Publisher's Note: The statements, opinions and data contained in all publications are solely those of the individual author(s) and contributor(s) and not of MDPI and/or the editor(s). MDPI and/or the editor(s) disclaim responsibility for any injury to people or property resulting from any ideas, methods, instructions or products referred to in the content.